

1 Assimilation of sea surface temperature, sea ice concentration and
2 sea ice drift in a model of the Southern Ocean

3 Alexander Barth^a, Martin Canter^a, Bert Van Schaeybroeck^b, Stéphane Vannitsem^b,
4 François Massonnet^c, Violette Zunz^c, Pierre Mathiot^d, Aida Alvera-Azcárate^a, Jean-Marie
5 Beckers^a

6 ^a*GeoHydrodynamic and Environmental Research (GHER), University of Liège, Liège, Belgium*

7 ^b*Koninklijk Meteorologisch Instituut (KMI), Brussels, Belgium*

8 ^c*Georges Lemaitre Centre for Earth and Climate Research, Earth and Life Institute, Université catholique
9 de Louvain, Louvain-la-Neuve, Belgium*

10 ^d*British Antarctic Survey, Natural Environment Research Council, Cambridge, UK*

11 **Abstract**

Current ocean models have relatively large errors and biases in the Southern Ocean. The aim of this study is to provide a reanalysis from 1985 to 2006 assimilating sea surface temperature, sea ice concentration and sea ice drift. In the following it is also shown how surface winds in the Southern Ocean can be improved using sea ice drift estimated from infrared radiometers. Such satellite observations are available since the late seventies and have the potential to improve the wind forcing before more direct measurements of winds over the ocean are available using scatterometry in the late nineties. The model results are compared to the assimilated data and to independent measurements (the World Ocean Database 2009 and the mean dynamic topography based on observations). The overall improvement of the assimilation is quantified, in particular the impact of the assimilation on the representation of the polar front is discussed. Finally a method to identify model errors in the Antarctic sea ice area is proposed based on Model Output Statistics techniques using a series of potential predictors. This approach provides new directions for model improvements.

12 *Keywords:* Ensemble Kalman Filter, data assimilation, sea ice drift, Model Output
13 Statistics, Southern Ocean

Email address: a.barth@ulg.ac.be (Alexander Barth)

URL: <http://modb.oce.ulg.ac.be/alex> (Alexander Barth)

14 1. Introduction

15 Observations of the sea ice extent in the Southern Ocean derived from satellite data display
16 a trend of 0.13 to 0.2 million km² per decade between November 1978 and December 2012
17 (Vaughan et al., 2013). Although the magnitude of this trend is subject to uncertainties
18 (e.g., Eisenman et al., 2014), the behavior of the Antarctic sea ice cover is in sharp contrast
19 with its Arctic counterpart which displays a decrease in sea ice extent over the last decades
20 (e.g., Turner and Overland, 2009). Several explanations have been proposed to account for
21 the slight increase in Antarctic sea ice extent but no consensus has been reached yet. Among
22 the proposed mechanisms, a potential link with the stratospheric ozone depletion has been
23 pointed out (Solomon, 1999) but this hypothesis is not compatible with recent analyses
24 (e.g., Bitz and Polvani, 2012; Smith et al., 2012; Sigmond and Fyfe, 2013). Changes in
25 the atmospheric circulation or in the ocean stratification may also have contributed to the
26 observed expansion of the sea ice cover (e.g., Zhang, 2007; Stammerjohn et al., 2008; Goosse
27 et al., 2009; Kirkman and Bitz, 2011; Landrum et al., 2012; Holland and Kwok, 2012; Bintanja
28 et al., 2013; Goosse and Zunz, 2014; de Lavergne et al., 2014). The internal variability of
29 the system, particularly strong in the Southern Ocean, may be responsible for the observed
30 positive trend in Antarctic sea ice extent as well (e.g., Mahlstein et al., 2013; Zunz et al.,
31 2013; Polvani and Smith, 2013; Swart and Fyfe, 2013).

32 Observations in the Southern Ocean are rather sparse in space and time. In particular,
33 reliable observations of the sea ice concentration are available from the late 1970's only (e.g.,
34 Parkinson and Cavalieri, 2012). In this context, climate models constitute adequate tools
35 to compensate for the lack of observations and investigate the processes that govern the
36 behavior of the sea ice cover around Antarctica. Coupled climate models are particularly
37 useful to analyze the interactions between the different components of the climate system.
38 Present-day general circulation models involved in the 5th Coupled Model Intercomparison
39 Project (Taylor et al., 2011) generally simulate a decrease in the Antarctic sea ice extent
40 over the last 30 years but a positive trend such as the observed one remains compatible
41 with the internal variability simulated by these models (e.g., Mahlstein et al., 2013; Zunz

42 [et al., 2013](#); [Polvani and Smith, 2013](#); [Swart and Fyfe, 2013](#)). Nevertheless, these models
43 often display systematic biases in their representation of the seasonal cycle or of the internal
44 variability (or both) of the Antarctic sea ice (e.g., [Turner et al., 2013](#); [Zunz et al., 2013](#)).
45 The reconstruction of the sea ice cover in the Southern Ocean provided by these models have
46 thus to be considered cautiously.

47 One way to more closely constrain the simulation of the ocean and the sea ice is to pre-
48 scribe the atmospheric conditions at the atmosphere/ocean–sea ice interface. These so-called
49 “forced” simulations resort generally to atmospheric reanalyses as boundary conditions, and
50 have been used extensively to study the past variability of the ocean and sea ice states
51 ([Fichefet and Morales Maqueda, 1999](#); [Fichefet et al., 2003](#); [Zhang, 2007](#); [Holland et al.,](#)
52 [2014](#)). It is clear the quality of these forced simulations is strongly dependent on that of the
53 atmospheric product utilized. Intercomparisons between different reanalysis products and
54 assessments against in-situ measurements all suggest that the reanalyzed atmospheric data
55 are subject to large uncertainties or systematic errors in the Southern Ocean ([Bromwich](#)
56 [et al., 2007](#); [Hines et al., 2000](#); [Vancoppenolle et al., 2011](#)) translating inevitably to the
57 ocean–sea ice system ([Timmerman et al., 2004](#); [Stössel et al., 2011](#)).

58 An even tighter constraint on the oceanic and sea ice states can be realized if observations
59 are used to update model estimates. Data assimilation has been an active area of research
60 in climate science. A limited number of studies have, however, attempted to implement data
61 assimilation in the Southern Ocean ([Stammer et al., 2002](#); [Stössel, 2008](#); [Massonnet et al.,](#)
62 [2013](#); [Ferry et al., 2012](#); [Balmaseda et al., 2008](#); [Carton and Giese, 2008](#); [Janjić et al., 2012](#))
63 where pressing scientific questions remain, though.

64 Implementing a data assimilation method in a large-scale ocean–sea ice model presents a
65 number of challenges as several methodological, statistical and physical questions are raised.
66 In theory, the background error statistics should be perfectly known in order for the data
67 assimilation to produce an optimal analysis. This is not feasible in practice, due to the
68 very high dimensionality of the state vector. For this reason, the true covariance matrix
69 of background errors is projected onto a space of much lower dimensionality and specified

70 either a priori (Ferry et al., 2012) or estimated on-the-fly (Sakov et al., 2012; Mathiot et al.,
71 2012) using a finite-size ensemble. For computational reasons, it is also common to assume
72 a diagonal structure for the observational error covariance matrix (i.e., uncorrelated errors)
73 while this is not necessarily the case in reality.

74 Most data assimilation methods also rely on statistical hypotheses. The gaussianity of
75 background and observational errors is often assumed, but rarely fulfilled. Not only can
76 this lead to sub-optimal updates, this can also lead to physical inconsistencies. Resorting
77 to the transformation of variables (e.g. Bertino et al., 2003; Simon and Bertino, 2009; Béal
78 et al., 2010) can be a first step, but it only acts on the marginal, and not multivariate
79 probability distribution functions. Likewise, since the background statistics are boiled down
80 to the covariance matrix, the update of non-assimilated fields follows their linear relationship
81 with the observable; this may result in an unphysical or imbalanced state after the update
82 in regions where strong nonlinearities are present, e.g. between sea surface temperature and
83 sea ice concentration (Lisæter et al., 2003).

84 Last but not least, a central and non-trivial issue concerns the decision on what should
85 be estimated. While the state itself is commonly estimated for reanalysis purposes, the
86 methods can be extended to the estimation of model bias to identify systematic errors (Sakov
87 et al., 2012), to the estimation of model parameters to partly reduce such systematic errors
88 (Massonnet et al., 2014) and ultimately to surface forcing estimation (Barth et al., 2011;
89 Marmain et al., 2014; Ngodock and Carrier, 2014). The estimation of atmospheric forcing
90 in the Southern Ocean has, to our knowledge, not been explored. Because Antarctic sea ice
91 trends are largely controlled by the wind forcing (Kimura, 2004; Holland and Kwok, 2012), it
92 seems natural to improve the representation of ice drift in the model. We propose to correct
93 the wind forcing using satellite sea ice drift data, taking advantage of the strong relationship
94 between sea ice drift and the wind field.

95 A first set of preliminary experiments have shown the difficulty to assimilate ice drift in a
96 coupled ocean-sea ice model. Sea ice drift is strongly related to the wind forcings (Kimura,
97 2004; Holland and Kwok, 2012) with a temporal scale of the order of days (about 4 days

98 based on the autocorrelation). The memory of the sea ice drift is thus relatively short. The
99 corresponding time scale is in fact more similar to the temporal scale of the atmospheric
100 variability than the temporal scale of ocean mesoscale circulation (order of weeks). This
101 short scale would require in principle a very frequent assimilation of sea ice drift data to
102 adequately resolve its underlying time-scale. However, a too frequent assimilation can
103 deteriorate the model results (*e.g.* Malanotte-Rizzoli et al., 1989; Barth et al., 2007; Yan
104 et al., 2014). To improve sea ice drift in the model, we therefore propose to correct the wind
105 forcing. This is possible due to the strong relationship between wind field and sea ice drift
106 (Holland and Kwok, 2012).

107 The objective of the study is to propose a methodology to use surface drift observations to
108 constrain an ocean-sea ice large-scale circulation model. We also aim to test this approach in
109 combination with sea surface temperature and sea ice concentration assimilation in a decadal
110 simulation and to assess the quality of the results with independent data. This study also
111 outlines an approach to evaluate the presence of model errors at the forecast step of the data
112 assimilation and to identify their potential sources

113 The ocean model is introduced in section 2 and then the used observations along with their
114 error covariance are discussed (section 3). The procedure adopted to correct the wind field
115 is detailed and validated in section 4. The data assimilation implementation is discussed
116 in section 5 and the results of the reanalysis are then presented and validated (section 6).
117 In the last section, post-processing techniques are used to relate forecast errors in sea ice
118 coverage with model errors associated with the dynamics of sea surface temperature.

119 2. Model

120 The primitive-equations model used in this study is NEMO (Nucleus for European Modelling
121 of the Ocean, Madec (2008)), coupled to the LIM2 (Louvain-la-Neuve Sea Ice Model) sea
122 ice model (Fichefet and Morales Maqueda, 1997; Timmermann et al., 2005; Bouillon et al.,
123 2009). The global ORCA2 implementation is used, which is based on an orthogonal grid with
124 a horizontal resolution of the order of 2° and 31 z-levels (Mathiot et al., 2011; Massonnet
125 et al., 2013). The hydrodynamic model is configured to filter free surface gravity waves by

126 including a damping term. The leap-frog scheme uses a time step of 1.6 hours for dynamics
 127 and tracers. The model is forced using air temperature and wind from the NCEP/NCAR
 128 reanalysis (Kalnay et al., 1996). Relative humidity, cloud cover and precipitation are based
 129 on a monthly climatological mean. The sea surface salinity is relaxed towards climatology
 130 with a fresh water flux of -27.7 mm/day times the salinity difference in psu.
 131 As in the following the link between sea ice drift and wind stress is studied, only the equation
 132 for sea ice drift is given here. The sea ice drift \mathbf{u} is governed by the momentum equation where
 133 the advection of momentum is neglected by scale analysis (Fichefet and Morales Maqueda,
 134 1997):

$$m \frac{\partial \mathbf{u}}{\partial t} = -mf \mathbf{e}_z \wedge \mathbf{u} + \boldsymbol{\tau}_{ai} + \boldsymbol{\tau}_{wi} - mg \nabla \zeta + \mathbf{F} \quad (1)$$

135 where m is the mass of the snow-ice system, f is the Coriolis parameter, \mathbf{e}_z is a unit vector
 136 pointing upward, $\boldsymbol{\tau}_{ai}$ (resp. $\boldsymbol{\tau}_{wi}$) denotes the drag with air (resp. water), g is the acceleration
 137 due to gravity, ζ is the surface elevation and \mathbf{F} the force due to the variation of internal
 138 stresses. For the complete model equations, the interested reader is referred to Madec (2008);
 139 Fichefet and Morales Maqueda (1997); Goosse and Fichefet (1999).

140 3. Observations

141 Global foundation sea surface temperature from OSTIA (Operational Sea Surface Temper-
 142 ature and Sea Ice Analysis Roberts-Jones et al., 2012) at an original resolution of 0.05° was
 143 reduced to a resolution of 2° by averaging all temperature values within a 2° by 2° grid cell.
 144 This data set also provides an error standard deviation (varying in space and time). Since
 145 information about the length scales over which the SST errors are correlated are lacking,
 146 the error standard deviation is also reduced to a resolution of 2° by simply averaging the
 147 standard deviations of all values with a 2° by 2° grid cell (averaging the standard deviation
 148 instead of the variances corresponds to the case of perfectly correlated errors, which is more
 149 appropriate since the OSTIA data set is relatively smooth).

150

151 Global sea ice fraction from the EUMETSAT Ocean and Sea Ice Satellite application Facility
152 (OSI-SAF [Roberts-Jones et al., 2012](#)) was also reduced to a resolution of 2° and assimilated
153 with an error standard deviation of 0.1. The OSTIA sea surface temperature and the OSI-
154 SAF sea ice fraction are distributed by MyOcean. Daily sea ice drift from NSIDC (National
155 Snow and Ice Data Center) is also assimilated in the ocean model. The sea ice drift is
156 based on data from the Advanced Very High Resolution Radiometer (AVHRR), Scanning
157 Multichannel Microwave Radiometer (SMMR), Special Sensor Microwave/Imager (SSM/I),
158 and International Arctic Buoy Programme (IABP) data ([Fowler, 2003](#)). The ice drift is
159 derived from the satellite data by maximizing the correlation of groups of pixels between
160 image pairs. We use version 1 of this data set which does not include derived ice drift
161 based on NCEP wind reanalysis (unlike the version 2 of the gridded and combined ice drift
162 data set). As the focus of this study is the Antarctic Ocean, only data from the southern
163 hemisphere is used. The error standard deviation for the assimilation is assumed to be 0.1
164 m/s. The value of this parameter was determined by a series preliminary experiments to find
165 the right balance between correcting as much as possible the sea ice drift without degrading
166 unobserved variables. The sea ice drift is used at two stages in our study: first it is used to
167 adjust the wind fields and, at a later stage, is used during the analysis to correct the model
168 state vector. This approach has been adopted as errors in the wind field and errors in the
169 ocean circulation manifest themselves in the model sea ice drift (and not only error in the
170 wind field). Experiments with different values of the standard deviation of the global sea ice
171 fraction error and sea ice drift error were also conducted as detailed in section [5.5](#).

172 **4. Wind field adjustment**

173 Errors in the sea ice drift can be attributed either to errors in the winds fields or to error
174 in the ocean currents. As winds and currents have two very different time scale, a two-step
175 approach was adopted. First, the wind fields are adjusted using sea ice drift as described in
176 this section. In a second step the sea ice drift is assimilated into the ocean-sea ice model in
177 order to reduce errors due to the ocean currents (section [5](#)).

178 *4.1. Relation between sea ice drift and wind*

179 The model sea ice drift is strongly related to the used wind forcing. To quantify the relation-
 180 ship between sea ice drift and wind fields, the complex correlation coefficient (Kundu and
 181 Allen, 1976) between the daily NEMO-LIM sea ice drift $(u_{\text{ice}}, v_{\text{ice}})$ and daily NCEP winds
 182 $(u_{\text{wind}}, v_{\text{wind}})$ has been computed by introducing the following complex variables ($i^2 = -1$):

$$\begin{aligned} w_{\text{ice}} &= u_{\text{ice}} + i v_{\text{ice}} \\ w_{\text{wind}} &= u_{\text{wind}} + i v_{\text{wind}} \end{aligned}$$

183 In order to maximize the correlation, we correlate the sea ice drift with different transforma-
 184 tions of the wind field. More specifically, we use different combinations of shifts and filters
 185 in time of the wind field. We use a time filter because we anticipate the sea ice drift to have
 186 a certain inertia and thus a memory of previous winds. The time shift and the temporal
 187 scale of the filter will be determined later. The time filter is implemented using an itera-
 188 tive diffusion scheme using a forward Euler step and a 2nd-order center diffusion operator
 189 (Alvera-Azcárate et al., 2009). The complex correlation coefficient between sea ice drift and
 190 filtered and shifted wind fields is given by:

$$\gamma = \frac{\langle \overline{w_{\text{ice}}} w_{\text{wind}} \rangle}{\sqrt{\langle \overline{w_{\text{ice}}} w_{\text{ice}} \rangle \langle \overline{w_{\text{wind}}} w_{\text{wind}} \rangle}}$$

191 The over-line denotes the complex conjugate and the angular brackets an average over time.
 192 The absolute value of the complex correlation coefficient is maximized by changing the
 193 timeshift and time-filter. The complex regression coefficient r derives an empirical relation-
 194 ship between the sea ice drift and the wind field. This relationship will be used later for
 195 wind field adjustment.

$$r = \frac{\langle \overline{w_{\text{ice}}} w_{\text{wind}} \rangle}{\langle \overline{w_{\text{ice}}} w_{\text{ice}} \rangle}$$

196 The complex correlation and regression coefficients are used instead of the (real) correla-
 197 tion/regression coefficient derived on the zonal and meridional component individually be-
 198 cause the complex coefficients can represent a rotation by a constant angle between the two

199 vectors (as a result for the Coriolis force) and is thus commonly used to analyze horizontal
200 velocities (*e.g.* Kundu and Allen, 1976; Barth et al., 2008).

201 The correlation analysis showed a strong correlation with magnitude of 0.9363 and a phase
202 of -19.52° between sea ice drift and 3-day average wind fields (panel (a) of Figure 1). This
203 phase (which is also the phase of the complex regression coefficient) represents the angle
204 between the sea ice drift vector and the wind vector. The maximum value was obtained
205 with no time lag. These results did not confirm the initial expectation of a time lag between
206 wind and sea ice drift as one could assume that the wind (the cause) precedes sea ice drift
207 (the effect). The maximum of the correlation as a function of the time lag is very well defined
208 while the correlation as a function of the filtering time scale is a bit flatter (panel (b) and
209 (c) of Figure 1). A scatter plot of wind versus sea ice drift using the optimal parameters
210 (filtering time scale and time lag) shows a good correspondence (Figure 2).

211 This strong relationship has been used to correct the surface winds. The general approach
212 is to use the regression coefficient to transform the observed sea ice drift as pseudo wind
213 observations and to attempt to improve zonal and meridional wind fields components. In
214 particular the following procedure has been adopted to compute the adjusted wind field:

- 215 • the first guess wind field is the NCEP reanalysis
- 216 • the model is run with this wind field (here for the year 2000)
- 217 • the sea ice drift error is calculated by comparing model with observed sea ice drift
- 218 • the sea ice drift error is transformed to “wind increment” using the regression coefficient
219 r
- 220 • “wind increment” is analyzed with the tool divand (detailed in the next section) on
221 the ORCA grid and the first guess (the NCEP reanalysis) is added

222 While other calibration experiment are carried out for the year 1985, the wind field
223 adjustments are first tuned for the year 2000 due to the availability of the Cross-
224 Calibrated Multi-Platform (CCMP) Ocean Surface Wind Vector Analyses (Atlas et al.,
225 2011) which will be used to independently validate the results.

226 *4.2. Spatial analysis with divand*

227 The sea ice drift provides only information about the wind field where the model has ice.
 228 However, if the sea ice drift indicates that the model should be corrected at a particular
 229 location, one can expect that it should also be corrected in a similar way at neighboring
 230 grid cells (even if they are not covered by ice). The tool divand (Barth et al., 2014) (Data
 231 Interpolating Variational Analysis in n-dimensions) is used to spatially interpolate the “wind
 232 increment” derived from the sea ice drift on the full ORCA2 grid. This tool is similar to
 233 the variational analysis DIVA (Brasseur et al., 1996) but this latter works on a triangular
 234 mesh. The DIVA tool cannot represent a periodic domain as is the case with the NEMO
 235 grid. Therefore the new tool divand was adapted to operate directly on a structured model
 236 grid with periodic boundary conditions.

237 For variational analyses, one requires that the analyzed field φ (here the wind increment)
 238 must be close to the N_d observations d_j ($j = 1, \dots, N_d$) and “smooth”. This is quantified
 239 using a cost function J :

$$J[\varphi] = \sum_{j=1}^{N_d} \mu_j [d_j - \varphi(\mathbf{x}_j)]^2 + \|\varphi\|^2 \quad (2)$$

240 Each observation has a weight μ_j which is directly related to its error variance. Abrupt
 241 variations of the analysis field are penalized using a regularization constraint (as in norm
 242 spline interpolation):

$$\|\varphi\|^2 = \frac{1}{c} \int_D \phi^2 + 2 \left(\tilde{\nabla} \phi \right) \cdot \left(\tilde{\nabla} \phi \right) + \left(\tilde{\nabla}^2 \phi \right)^2 dx \quad (3)$$

243 The normalization coefficient c is set to 4π to ensure that the background covariance matrix
 244 has a unit variance (Brasseur et al., 1996). The data weight μ_j represents the ratio of the
 245 error variance of the background NCEP field and the error variance of the observation.

246 The correlation length L is introduced by scaling the differential operator for gradient and
 247 Laplacian:

$$\begin{aligned}\tilde{\nabla} &= L\nabla \\ \tilde{\nabla}^2 &= \nabla \cdot (L^2\nabla)\end{aligned}$$

248 Here the correlation length is a scalar, but it can also be a diagonal matrix in the previ-
 249 ous equation if the length scale is different for the zonal and meridional dimensions. The
 250 regularization constraint guarantees that the interpolated field and its first order derivative
 251 (such as the wind curl) is continuous.

252 An estimation of the background NCEP error standard deviation is necessary to define
 253 the data weight μ_i . In the present case, the pseudo observation (the wind information
 254 derived from the sea ice drift observation) error standard deviation is derived using the error
 255 standard deviation of the sea ice drift. The remaining parameter of the analysis, namely the
 256 correlation length scale and background NCEP error standard deviation, will be determined
 257 in the following. The correlation length controls the distance over which the information
 258 from the pseudo-wind observation is extrapolated spatially and the NCEP error standard
 259 deviation determines how close the analyzed field has to come to these pseudo-observations.

260 *4.3. Calibration*

261 The correlation length is varied from 300 km to 5000 km and the standard deviation error
 262 is varied from 0.1 m/s to 10 m/s. For each parameter 10 values are tested. These values
 263 are uniformly distributed in logarithmic space. For each of these parameters, the divand
 264 analysis is performed and the NEMO-LIM2 model is run simulating the year 2000 with the
 265 adjusted wind fields. Besides the momentum equation, the norm of the adjusted wind field
 266 is also used in the heat flux computation via the bulk formulas (which is a separate input
 267 file for NEMO).

268 Figure 3 shows the RMS error between the model sea ice drift obtained using the adjusted
 269 wind and the observed sea ice drift. This is not an independent validation since the observed
 270 sea ice drift is used to adjust the wind fields. This comparison is rather a confirmation
 271 that the adjustment works as expected. The RMS error between the model sea ice drift

272 and observations is 0.1235 m/s with original (i.e. non-adjusted) NCEP forcing. The RMS
273 error is indeed reduced thanks to the adjustment (Figure 3) and, as expected, the lowest
274 RMS error is obtained when using a large value of the standard deviation of the NCEP wind
275 error. In this case, the adjusted wind will thus be forced to come closer to the pseudo-wind
276 observations (based on sea ice drift).

277 As an independent comparison the CCMP Ocean Surface Wind Vector Analyses (Atlas et al.,
278 2011) based on ERA-40 and observations such as QuickScat for the year 2000 south of 60°S
279 is used. Sea ice drift is not used in the CCMP product. For every tested correlation length
280 scale and NCEP error standard deviation, the RMS error between the adjusted wind and
281 the CCMP wind field is computed (Figure 3, panel b). This comparison shows that the
282 wind field is indeed improved using the sea ice drift measurements. As before, the general
283 tendency is that the RMS difference between the adjusted winds and CCMP winds decreases
284 as the error standard deviation increases. This comparison shows that the optimal range of
285 the correlation length scale is between 500 km and 1500 km.

286 The model sea ice concentration obtained by the adjusted wind is also compared to the
287 OSTIA/OSI-SAF observations (Figure 3, panel c). In general the sea ice concentration
288 varies only weakly by changing the parameter of the analysis. This suggests that only a
289 small part of the RMS error in sea ice concentration can be attributed to the wind forcing
290 and that sea ice concentration is mostly driven by thermodynamic forcings. Contrary to the
291 previous comparison the error slightly increases for large values of the NCEP error standard
292 deviation.

293 Overall a large value of the background error improves sea ice drift and reduces the RMS
294 error in comparison with CCMP winds but it degrades the sea ice concentration (if error
295 standard deviation is larger than 5 m/s). Correlation lengths between 500 km and 1000
296 km give acceptable results. By combining the results from the different comparisons, the
297 wind fields have been adjusted using a correlation length of 700 km and a background error
298 standard deviation of 2 m/s.

299 The adjustment procedure has been applied to the wind field time series from 1985 to 2006.

300 The average wind vector over this period has been computed (Figure 4). The most signifi-
301 cant change occurs near the coast where the adjustment generally increase the offshore wind
302 and decreases (the generally negative) zonal wind component. Those changes are consistent
303 with the changes from low to high resolution atmospheric models (Mathiot et al., 2010) and
304 are attributed to katabatic winds which are important to the formation of polynyas (Mas-
305 som et al., 1998; Morales Maqueda et al., 2004). As the wind curl is an important forcing
306 for Ekman pumping it has been computed for the original and adjusted wind in order to
307 determine the effects on the wind curl. The most important changes in the wind curl (in
308 term of the RMS error) have been applied in the Weddell and Ross Seas (panel (b) of Figure
309 5). Even in these areas the RMS difference is still smaller by a factor of 2 to 3 than the
310 standard deviation of the wind curl (panel (a) of Figure 5).

311

312 For the year 2006, a problem in version 1 of the NSIDC ice drift product has been identified
313 for the Arctic sea ice drift (Sumata et al., 2014). However the authors of this study did
314 not analyse the ice-drift in the Southern Hemisphere. The comparison of the free-running
315 model with the Antarctic ice drift did not reveal a sudden change in the RMS error for the
316 year 2006. However, wind field corrections based on version 2 of the NSIDC ice drift data
317 (using only Advanced Very High Resolution Radiometer (AVHRR), Scanning Multichannel
318 Microwave Radiometer (SMMR), Special Sensor Microwave/Imager (SSM/I) but not NCEP
319 wind field data), could reduce the RMS error of the wind field compared to CCMP could by
320 7% compared to version 1 of the NSIDC ice drift.

321 5. Data assimilation

322 The implemented data assimilation scheme is the Ensemble Transform Kalman Filter (Bishop
323 et al., 2001). In ensemble-based assimilation schemes, the error statistics of the model
324 state vector is estimated by perturbing uncertain aspects of the model. In the present
325 configuration we perturb surface winds (10 m) and surface air temperature (2 m). The
326 adjusted wind from the previous section are used. Atmospheric parameters coming from
327 climatology are not perturbed. The data assimilation scheme employs an ensemble with

328 50 members. Observations are assimilated every 5 days which is a compromise between
 329 available computer resources and maximizing the usage of the observations.

330 5.1. Perturbed forcings

331 The perturbation scheme is based on a Fourier decomposition. Formally all perturbed vari-
 332 ables are grouped into a time-dependent vector:

$$\mathbf{x} = (u_{\text{air}} \ v_{\text{air}} \ T_{\text{air}})^T \quad \text{at all grid points} \quad (4)$$

333 A Fourier decomposition of the NCEP wind vectors and air temperature over the time
 334 domain is performed (Barth et al., 2011; Marmain et al., 2014):

$$\mathbf{x}(t) = \sum_k \mathbf{a}_k \exp(i\omega_k t), \quad (5)$$

335 where ω_k is the k -th angular frequency (positive or negative) and \mathbf{a}_k are complex spatial
 336 vector fields corresponding to the Fourier coefficients of the angular frequency ω_k (Δt is here
 337 24 hours):

$$\omega_k = \frac{2\pi k}{\Delta t} \quad k = -\frac{k_{max}}{2}, \dots, \frac{k_{max}}{2} - 1 \quad (6)$$

338 where k_{max} is the number of Fourier modes. Using the spatial and multivariate structure of
 339 the Fourier modes \mathbf{a}_k , perturbations $\mathbf{x}'(t)$ are constructed by:

$$\mathbf{x}'(t) = \alpha \operatorname{Re} \left(\sum_k \mathbf{a}_k z_k(t) \right), \quad (7)$$

340 where z_k is a complex random time series with a temporal correlation scale of $T_k = 2\pi/|\omega_k|$,
 341 zero mean and unit variance. The value of α is determined by ensemble simulations with
 342 perturbed forcings to ensure that the resulting ensemble spread is comparable to the expected
 343 error of the model.

344 Only Fourier modes with a time period between 20 and 70 days are used for the perturbations
 345 in order to exclude the seasonal variations (which have a large variance and whose amplitude
 346 is not representative for its expected error) and short-scale variations which are not the

347 primary focus of this study. Since the perturbation scheme is multivariate, the same range
 348 of time scales is used to perturb wind and air temperature. The real and imaginary parts of
 349 the random time series have the following covariance $C_T(t, t')$:

$$C_T(t, t') = e^{-\frac{(t-t')^2}{T_k^2}} \quad (8)$$

350 These perturbations have been added to the first guess estimate:

$$\mathbf{x}^{(l)} = \mathbf{x} + \mathbf{x}'^{(l)} \quad (9)$$

351 where l is the index of the ensemble member. The perturbation scheme is similar to pertur-
 352 bations generated by Empirical Orthogonal Functions (EOF; *e.g.* [Vandenbulcke et al., 2008](#);
 353 [Béal et al., 2010](#)). The advantage of perturbations proportional to a Fourier mode is that it
 354 is easier to associate a time scale to a Fourier mode than to an EOF. The wind perturbations
 355 have a magnitude similar to the wind correction derived in the previous section. However,
 356 the wind perturbations have a zero mean so that the wind corrections are still relevant for
 357 the whole ensemble (and in particular its mean state).

358 As the wind speed is an independent forcing field for NEMO, the perturbed wind speed is
 359 computed for each ensemble member:

$$\|\mathbf{u}_{\text{air}}^{(l)}\| = \sqrt{u_{\text{air}}^{(l)2} + v_{\text{air}}^{(l)2}} \quad (10)$$

360 The perturbation scheme (without assimilation) is illustrated for the year 2007. Figure 6
 361 shows the ensemble standard deviation of the wind speed for a particular day (2007-02-
 362 21). The ensemble standard deviation is high near the polar regions where time variability
 363 (between 20 and 70 days) is relatively large. The same behaviour was also seen in the air
 364 temperature (not shown). Figure 7 shows the globally-averaged ensemble spread for one-year
 365 of spin-up. The spread in SST stabilized relatively fast after 2 months of simulation. Globally
 366 the uncertainty of the ensemble SST is about 0.8 °C which is of the order of magnitude of the
 367 model error in SST. A meaningful correction of the model state can only occur at locations
 368 where the model develops a sufficient ensemble spread. The spread of sea ice concentration

369 was computed for the period of minimum and maximum sea ice extent (Figure 8). For the
370 minimum sea ice extent period, a spread of 0.3 or larger was generated except in the eastern
371 part where nearly all sea ice has melted. During the maximum sea ice extent, areas with
372 significant ensemble spread form a ring structure. All ensemble members have no sea ice
373 outside this ring and are essentially completely sea ice covered inside this ring. The width
374 of this ring represents the uncertainty of the sea ice edge.

375 Ensemble simulations have also been carried out with only air temperature perturbations
376 and only wind field perturbations in order to determine the impact of those error sources
377 individually. Figure 9 shows the resulting ensemble variance after a one-year ensemble spin-
378 up for ice concentration and ice drift variance. The air temperature perturbations generate
379 a relatively uniform ensemble spread while the wind perturbations enhance the ensemble
380 spread mostly near the coastline. As expected, the ice drift variance (computed only over
381 model grid points with nonzero ice concentration) does not respond to the air temperature
382 perturbations, but it responds quite significantly to the wind field perturbations. The impact
383 is strongest in the open ocean where the ice movement is not constrained by the coast. The
384 combined effect of air temperature and wind perturbations is relatively close to the sum
385 of both perturbations individually which indicates that the wind field and air temperature
386 perturbations as well as their response in the model are relatively independent from each
387 other even after a one-year ensemble simulation.

388 *5.2. State vector*

389 In data assimilation, all model variables to be corrected by the observations are gathered
390 in the state vector which is here composed of various hydrodynamic and sea ice variables.
391 It includes the horizontal velocity components, temperature, salinity, surface elevation, curl
392 of horizontal velocity components, divergence of horizontal velocity components, turbulent
393 kinetic energy and barotropic stream function trends. Those variables are necessary to restart
394 NEMO. Some of these variables are interdependent as the horizontal velocity components
395 are directly related to their divergence and curl. However since the link is linear, the analysis
396 will preserve their relationship. As the model uses a leap-frog time step, two time instances

397 of these variables are included in the state vector.

398 For the sea ice model, sea ice concentration, sea ice thickness, the horizontal sea ice-velocity
399 components, snow thickness and temperature inside the ice/snow layer (at three layers) are
400 included in the state vector. The sea ice concentration was transformed with a Gaussian
401 anamorphosis (see section 5.3). In total, the state vector contains 28 different variables and
402 about 6 million elements (all variables combined).

403 A set of experiments was conducted with a reduced state vector, where the snow thickness
404 and temperature inside the ice/snow layer was not corrected by the assimilation in order to
405 determine if the assimilation has a beneficial impact on these variables.

406 5.3. Gaussian anamorphosis

407 The Kalman filter analysis provides the most likely state if errors are Gaussian-distributed.
408 However some variables are clearly not Gaussian-distributed, in particular sea ice concen-
409 tration which is bound between 0 and 1. A linear analysis scheme can produce unrealistic
410 values outside of this range. Gaussian anamorphosis (Bertino et al., 2003; Lenartz et al.,
411 2007; Simon and Bertino, 2009; Béal et al., 2010) consists of applying a non-linear transfor-
412 mation onto the model variable which should make the pdf of the state vector more similar
413 to a Gaussian pdf. In practice such transformations are applied to individual elements of
414 the state vector and thus operating only on the marginal distribution and not on the full
415 multidimensional pdf. Such transformations can be based on an analytic transformation
416 (e.g. logarithm, for lognormal distributions) or empirically based on the distribution of the
417 observations.

418 The initial distribution of sea ice concentration is estimated from a 1-year free-running
419 ensemble simulation. The derived transformation function is here independent in time and
420 space (Figure 10). The anamorphosis transform was applied to all ensemble members so
421 that the ensemble members include the transformed sea-ice concentration. Observed sea ice
422 concentration was not transformed, therefore the observation operator includes the inverse
423 anamorphosis transform and is non-linear. This approach allows to define the error standard
424 deviation of the observations in the original units. The analysis scheme is implemented with

425 the non-linear observation operator as described in [Chen and Snyder \(2007\)](#) and [Barth et al.](#)
 426 [\(2011\)](#).

427 Other model variables exhibit a non-Gaussian behavior too as thickness of snow and sea ice
 428 layers (which have to be positive) and sea water temperature (which has to be above the
 429 freezing temperature). We limit ourselves to sea ice concentration as this is an observed
 430 variable and thus large corrections are expected for this parameter. Other variables with a
 431 non-Gaussian distribution are dealt with using an ad-hoc correction after the analysis step.

432 5.4. Analysis

433 The analysis scheme is based on the Kalman filter analysis, where the model forecast \mathbf{x}^f (with
 434 error covariance \mathbf{P}^f) is updated by the observation \mathbf{y}^o (with error covariance \mathbf{R}) resulting in
 435 the analysis state \mathbf{x}^a and its error covariance (\mathbf{P}^a):

$$\mathbf{x}^a = \mathbf{x}^f + \mathbf{K} (\mathbf{y}^o - \mathbf{H}\mathbf{x}^f) \quad (11)$$

$$\mathbf{K} = \mathbf{P}^f \mathbf{H}^T (\mathbf{H}\mathbf{P}^f \mathbf{H}^T + \mathbf{R})^{-1} \quad (12)$$

$$\mathbf{P}^a = \mathbf{P}^f - \mathbf{K}\mathbf{H}\mathbf{P}^f \quad (13)$$

436 where \mathbf{H} is the observation operator extracting the observed part of the state vector. The
 437 mean state \mathbf{x}^f and its covariance are computed from an ensemble of perturbed members
 438 $\mathbf{x}^{f(k)}$ where $k = 1, \dots, N$ ([Evensen, 2007](#)):

$$\mathbf{x}^f = \frac{1}{N} \sum_{k=1}^N \mathbf{x}^{f(k)} \quad (14)$$

$$\mathbf{P}^f = \frac{1}{N-1} \sum_{k=1}^N \left(\mathbf{x}^{f(k)} - \overline{\mathbf{x}^f} \right) \left(\mathbf{x}^{f(k)} - \overline{\mathbf{x}^f} \right)^T = \mathbf{S}^f \mathbf{S}^{fT} \quad (15)$$

439 where the columns of the matrix \mathbf{S}^f are the difference between each member and the ensemble
 440 mean (multiplied by $\frac{1}{\sqrt{N-1}}$). The ensemble update used here is based on the Ensemble
 441 Transform Kalman Filter ([Bishop et al., 2001](#)). In order to avoid to form \mathbf{P}^a explicitly, \mathbf{P}^a

442 is expressed also in terms of the square root matrix \mathbf{S}^a ($\mathbf{P}^a = \mathbf{S}^a \mathbf{S}^{aT}$) which is possible when
 443 the following eigenvalue decomposition is made:

$$(\mathbf{H}\mathbf{S}^f)^T \mathbf{R}^{-1} \mathbf{H}\mathbf{S}^f = \mathbf{U}\mathbf{\Lambda}\mathbf{U}^T \quad (16)$$

444 where $\mathbf{U}^T \mathbf{U} = \mathbf{I}$ and where $\mathbf{\Lambda}$ is diagonal. \mathbf{U} and $\mathbf{\Lambda}$ are both of size $N \times N$.

445

446 Using this eigenvector decomposition and the Sherman-Morrison-Woodbury formula (Golub
 447 and Van Loan, 1996) one can compute the analysis \mathbf{x}^a and the square root of the analysis
 448 error covariance \mathbf{S}^a by:

$$\mathbf{x}^a = \mathbf{x}^f + \mathbf{S}^f \mathbf{U} (\mathbf{I} + \mathbf{\Lambda})^{-1} \mathbf{U}^T (\mathbf{H}\mathbf{S}^f)^T \mathbf{R}^{-1} (\mathbf{y}^o - \mathbf{H}\mathbf{x}^f) \quad (17)$$

$$\mathbf{S}^a = \mathbf{S}^f \mathbf{U} (\mathbf{I} + \mathbf{\Lambda})^{-1/2} \mathbf{U}^T \quad (18)$$

449 Based on \mathbf{x}^a and \mathbf{S}^a , an ensemble can be finally reconstructed:

$$\mathbf{x}^{a(k)} = \mathbf{x}^a + \sqrt{N-1} \mathbf{S}^a \mathbf{e}^{(k)} \quad (19)$$

450 In order to filter spurious long-range correlations, a localization scheme in the observation
 451 space has been used with a length scale of 2000 km (approximately 20 grid points). This
 452 assimilation scheme is implemented in a tool called the Ocean Assimilation Kit and described
 453 in more detail in Vandenbulcke et al. (2006); Barth et al. (2008). The present setup is the
 454 first global implementation of the assimilation tool and it required some adaption in order
 455 to properly handle the periodic boundary conditions in the localization scheme.

456 5.5. Variant of assimilation experiments

457 Different assimilation experiments were conducted to assess the different choices that have
 458 been adopted during the implementation of the assimilation scheme. Table 1 shows the
 459 RMS error and skill-score of the model state forecast compared to the observations (not yet
 460 assimilated). The RMS values for SST and sea ice concentration are computed over the

461 entire globe. If the RMS values for sea ice concentration are to be compared with RMS
 462 values computed over the latitude range $[-90, -\phi]$ and $[\phi, 90]$, then the values reported here
 463 have to be multiplied by $1/(1 - \sin(\phi))$. The RMS values for the sea ice drift are computed
 464 only over the southern hemisphere over the grid cells where sea ice is present in the model
 465 and in the observations. These experiments were carried out for the year 1985 (the initial
 466 year of the study). The skill-score is defined as:

$$\text{skill score}(\text{experiment}) = 1 - \frac{\text{RMS}^2(\text{experiment})}{\text{RMS}^2(\text{baseline})} \quad (20)$$

467 Negative values of this skill score mean a deterioration of the results and positive values an
 468 improvement. The baseline experiment uses a state vector of 30 variables, Gaussian anamor-
 469 phosis is applied to sea ice concentration, and the standard deviation error for the sea ice
 470 concentration is set to 0.1. In a first test, the Gaussian anamorphosis was disabled and the
 471 sea ice concentration was adjusted to the interval $[0, 1]$ after the analysis (row ExpFNA-0.1
 472 in table 1). Compared to the baseline experiment, a small error increase in sea ice concen-
 473 tration was observed, while other variables are not affected. Given the strong non-Gaussian
 474 character of the sea ice concentration, one could have expected a larger impact of the anamor-
 475 phosis transform. However, the Gaussian anamorphosis only transforms the marginal pdfs
 476 while the character of the multidimensional pdf of the state-vector might not be significantly
 477 changed by the transformation. In the following experiments, the Gaussian anamorphosis
 478 was kept.

479

480 By reducing the error standard deviation (ExpFA-0.07) of the sea ice concentration to 0.07,
 481 the sea ice concentration forecast was improved by 8 % (compared to the baseline experiment
 482 with an error standard deviation of 0.1). A larger positive impact on the model variables (and
 483 especially on sea ice concentration) was obtained by using a reduced state vector excluding
 484 snow thickness and temperature inside the ice/snow layer (ExpRA-0.05, ExpRA-0.07 and
 485 ExpRA-0.1). This indicates that the excluded variables are related in a non-linear way to
 486 the observations and that relationship cannot be represented by a covariance. However, for

487 this experiment the best results were obtained by using again 0.1 as error standard deviation
488 of the sea ice concentration. Using a lower value did not result in an improvement contrary
489 to the result with the full state vector.

490 In summary, the experiments lead to the configuration with a reduced state vector and
491 Gaussian anamorphosis of sea ice concentration, where sea ice concentration was assimilated
492 with an error standard deviation of 0.1.

493 **6. Reanalysis**

494 While the calibration of the assimilation setup was performed on a single year (2000), this
495 section presents the model simulations with data assimilation from 1st January 1985 to 31st
496 December 2006. The time period was determined to ensure the availability of all used data
497 sets.

498 *6.1. RMS with assimilated data sets*

499 The comparison with the assimilated data set is instructive to get a first view of the be-
500 haviour of the assimilated variables. The RMS error for sea surface temperature and sea
501 ice concentration are computed over the whole globe while the RMS error for sea ice drift
502 is limited to the southern hemisphere. The free model is not influenced by the observation
503 described in section 3. In particular, its wind forcing is the original NCEP wind forcing. As
504 mentioned previously, the sea ice drift observations are used at two stages: for correcting
505 the wind forcing and during the analysis.

506

507 Since the RMS errors showed a clear seasonal behaviour the 1606 assimilation cycles were
508 aggregated on a monthly basis (Figure 11). In the free run, the sea surface temperature RMS
509 error is on average 0.98 °C. This error is strongly reduced after the first assimilation cycle (not
510 shown) and maintained at a relatively low level (about 0.5 °C) by the continuous assimilation
511 of SST data. On average, the SST RMS error is highest during August and a secondary peak
512 is observed in January. The seasonal behaviour of the SST RMS is significantly reduced by
513 the assimilation. The behaviour of the sea ice concentration is similar, as a clear seasonal

514 cycle can be seen in the RMS error and the average RMS error is highest in September
515 (the period with the maximum sea ice extent in the Southern Hemisphere). As expected
516 from the previous result, the RMS error of the sea ice drift component (only in the southern
517 hemisphere) shows also a strong seasonal cycle. While the model forecast RMS is still smaller
518 than the RMS of the free run, the RMS error increases relatively fast after the analysis (not
519 shown). This is attributed to the fact that the underlying time scales of the variability in
520 sea ice drift are shorter than the 5-day assimilation cycle. The average of the RMS error
521 over all assimilation cycles is given in table 2.

522 6.2. Validation with the World Ocean Database

523 All observations from the World Ocean Database from the period 1st January 1985 to 31st
524 December 2006 have been collected. For model verification, the model results are usually
525 interpolated on the location and date of the observations (*e.g.* [Alvera-Azcárate et al., 2007](#)).
526 As the vertical grid of the model is the same at every location, we decided to rather inter-
527 polate the observations vertically on the model levels. These vertically interpolated profiles
528 are then compared to the model results interpolated horizontally.

529

530 The free-running model has the largest temperature error near the surface where the model
531 has the most variability (Figure 12). As the model assimilates sea surface temperature,
532 the largest impact of the assimilation is indeed at the surface where the RMS error and
533 bias (which is partly included in the RMS error) are strongly reduced. The RMS error is
534 improved by the assimilation over 200 m depth and the bias over 120 m. Below those depths
535 there is a slight degradation of the temperature which is essentially a systematic error in
536 form of a bias. One possible way forward for improvement of the assimilation scheme could
537 be to include a temperature relaxation toward a climatology to control such error. As the
538 ensemble is generated by perturbing the atmospheric fields, the resulting vertical correlation
539 scale between the surface and the subsurface level is about 100 meters (as calculated by
540 computing the standard deviation averaged over time and horizontal space of the analysis
541 increment). As the error increase at depth is not introduced by the analysis step, it must be

542 introduced by the model reaction to an analyzed initial condition. In fact, it is well known
543 that sequential analysis can produce shocks after restarting the model from an analysis (*e.g.*
544 [Malanotte-Rizzoli et al., 1989](#); [Barth et al., 2007](#); [Yan et al., 2014](#)). Incremental update
545 techniques are a promising approach to reduce such problems during the re-initialization of
546 the model ([Bloom et al., 1996](#); [Yan et al., 2014](#)).

547 The model does not assimilate salinity and therefore changes in salinity are only due to
548 the multivariate covariance between the observed variables and salinity, and also due to the
549 model adjustment after the analysis. The validation reveals that the assimilation reduces
550 the salinity RMS error and bias everywhere with a diminishing impact at depth. Contrary
551 to the temperature validation, no degradation at depth was observed.

552 *6.3. Mean sea surface height*

553 The mean model sea surface height was also compared with CNES-CLS09 MDT version
554 1.1 ([Rio et al., 2011](#)). The model sea surface height is related to the mean currents by the
555 geostrophic relationship. The CNES-CLS09 MDT is essentially based on in situ dynamic
556 heights, drifting buoy velocities and the geoid model computed from GRACE (Gravity Re-
557 covery and Climate Experiment) data. It is thus an independent data set. The objective of
558 this comparison is to assess the impact of the assimilation on the mean sea surface height
559 and the mean currents. As the focus of this study is the southern polar region, the compar-
560 ison is limited to the area south of 40°S. A constant over this domain has been subtracted
561 to remove any offset which is not dynamically significant. The RMS values represent thus
562 centered RMS. The RMS error between the free running model and the MDT over this area
563 is 0.218 m which is reduced to 0.165 m between analysis and MDT. The RMS of the 5-day
564 forecast based on the analysis is essentially the same with 0.166 m ([Figure 13](#)). Overall the
565 mean SSH gradient is more realistic in the analysis compared to the free model run leading
566 to a more realistic representation of the Antarctic Circumpolar Current. The structure of the
567 gradient is also more realistic in the model run with assimilation, especially in the Amundsen
568 Sea and Ross sea sector.

569 Assuming a jet with a Gaussian velocity profile, one can determine the characteristics of the

570 polar front by fitting the error function on the mean sea surface height h (Gille, 1994):

$$h(y) = a + (b - a) \operatorname{erf} \left(\frac{y - p}{w} \right) \quad (21)$$

571 where y is the latitude, p is the position, w is the width, a and b are the hypothetical values
572 of the sea surface height if y could tend to $-\infty$ and $+\infty$ (respectively). Tests were performed
573 to include an additional term to separate the polar and the sub-polar front, however as SSH
574 corresponds to mean over a long time period and given the coarse resolution of the model
575 results, the sea surface height h did not contain sufficient details to distinguish these two
576 fronts. The proposed fit corresponds thus to the overall change of SSH over the frontal
577 system. This fit has been performed on the ORCA2 model grid (also for the CNES-CLS09
578 MDT) and repeated for all longitudes of the model grid. The model run without assimilation
579 reproduces relatively well the position of the front (Figure 14). The RMS error of the position
580 (averaged over all longitudes) is 1.70° . While the assimilation can locally degrade the position
581 of the front, it reduces on average the RMS error to 1.61° . The overall structure of the width
582 of the front agrees with the width determined from the CNES-CLS09 MDT. However, the
583 width in the free model run is overestimated, indicating that the model is too smooth and
584 the ACC (Antarctic Circumpolar Current) is too diffuse. While the width of the front in the
585 analysis is still too large, the assimilation improves its representation and the RMS error is
586 reduced from 5.96° to 3.27° .

587 7. Identification of model errors

588 The aim of this section is the proposal of a technique for the identification of model errors
589 during the assimilation cycle and its application on the proposed reanalysis for sea ice. Model
590 errors can be traced by considering how the data assimilation system tends to pull the anal-
591 ysis away from the background towards the observations. Such approach was pioneered by
592 Klinker and Sardeshmukh (1992) and further developed by Schubert and Chang (1996) and
593 by Rodwell and Palmer (2007). The problem is approached here from a different perspective
594 by the use of post-processing techniques and rigorous theoretical considerations. As argued

595 in [Vannitsem and Nicolis \(2008\)](#), forecasts at small lead times can be corrected using Model
 596 Output Statistics (MOS) techniques in case systematic model errors are present. Random
 597 initial-condition errors, on the other hand, cannot be corrected. Importantly, additional
 598 corrections can be obtained by consideration of an additional predictor (other than the one
 599 corresponding to the predictand) *in case this predictor is strongly correlated to the model*
 600 *error present*. The aim of this section is to diagnose the presence of model errors by seeking
 601 additional predictors that strongly correct the forecast. The identification of good predictors
 602 may then lead to an increased understanding of the source of error.

603 The data set considered consists of the ensemble-mean of the NEMO-LIM2 reanalysis. The
 604 observations against which we calibrate and compare the results are the aforementioned
 605 OSTIA data set.

606 *7.1. Correction based on post-processing techniques*

607 Three predictands or corrected forecasts are constructed: The *total Antarctic sea ice area*, the
 608 *Antarctic sea ice area as a function of longitude* and the *Antarctic sea ice area as a function*
 609 *of latitude*. Tests pointed out that the point-by-point or full-field sea ice concentrations could
 610 not be corrected with the post-processing methods. Full-field calibration methods based on
 611 EOF analysis might be an alternative that is worth investigating in the future ([Di Giuseppe](#)
 612 [et al., 2013](#)), but the present analysis is restricted to spatially integrated quantities.

613 The corrected forecast x^c is obtained by use of two predictors or model variables, x_1^f and x_2^f ,
 614 based on the following regression relation:

$$x^c = \theta \left(\beta_0 + \beta_1 x_1^f + \beta_2 x_2^f \right). \quad (22)$$

615 Here the function θ ensures that the corrected sea ice area x^c is nonnegative:

$$\theta(z) = z \text{ when } z \geq 0, \text{ and, } \theta(z) = 0 \text{ when } z < 0. \quad (23)$$

616 The regression coefficients β_0 , β_1 and β_2 are obtained by numerical minimization of the
 617 mean squared error, analogous to the technique of Linear Model Output Statistics (LMOS)

618 as discussed by Vannitsem and Nicolis (2008):

$$MSE = \langle (x_n^c - y_n^o)^2 \rangle_n, \quad (24)$$

619 where $\langle \cdot \rangle_n$ represents the average over the training data set and y^o denotes the observation.

620 Three correction methods are used here:

621 • *Bias correction*: $\beta_1 = 1$ and $\beta_2 = 0$ while β_0 is an optimized parameter.

622 • *One-predictor correction*: $\beta_2 = 0$ while β_0 and β_1 are optimized parameters.

623 • *Two-predictor correction*: β_0 , β_1 and β_2 are optimized parameters.

624 As the first predictor x_1^f the model variable corresponding to the predictand is taken. For
625 the second predictand x_2^f , on the other hand, the following variables are considered, all
626 taken from the 5-day forecast: ice thickness, ice y-velocity, ice x-velocity, sea surface height,
627 barotropic stream function trends, sea surface height mean, sea surface salinity mean, sea
628 surface temperature mean, sea surface x (meridional) and y (zonal) mean velocity, diver-
629 gence and rotational components of horizontal velocity components, salinity, temperature,
630 x-velocity, y-velocity and turbulent kinetic energy. As the model uses a leap-frog time step-
631 ping scheme, for some of the variable two consecutive time steps are available and have been
632 used as predictors. Extra second predictors are constructed by full-field transformations
633 of the aforementioned variables. More specifically, the totally advected, the longitudinally-
634 advected and latitudinally-advected quantities are obtained by multiplying the variables
635 with the total velocity or the longitudinal or latitudinal surface velocities, respectively. Also
636 full-field multiplications are performed with the sea ice concentration SIC, with 1-SIC and
637 with SIC(1-SIC) in order to obtain predictors that are only nonzero over sea ice, over open
638 sea or near the sea ice edge, respectively. For non-surface variables we consider also the
639 vertically-averaged (oceanic) quantities.

640 For correcting the predictand Antarctic sea ice area, all predictors are averages over the
641 oceanic area south of 50°S. Similarly the predictors tested to correct the predictands that
642 are a function of longitude or latitude are model variables averaged along the same latitudes

643 and longitudes, all south of 50°S. Note that for each of the three correction methods the
644 regression coefficients are calculated separately. Also, longitude-by-longitude (latitude-by-
645 latitude) analysis is performed for the predictands that are a function of longitude (latitude).
646 Verification scores are obtained by correcting data subsets that are independent from the ones
647 used to obtain the regression coefficients. More specifically, a cross validation is performed
648 by which each single calendar year is corrected using the coefficients that were trained on
649 the other 20 years.

650 7.2. Results of post-processing

651 The overall impact of all correction schemes on the Antarctic sea ice area is tabulated in
652 Table 3 showing in the first column the RMSE values of the corrected forecasts, relative
653 to the RMSE of the uncorrected 5-day forecast. Our post-processing technique was also
654 applied on the analysis data (taking $x^f \rightarrow x^a$ in Eq. (22)) for which results are shown in the
655 right-most column of Table 3.

656
657 A bias correction of the forecast amounts to a 5% RMSE reduction as compared to the
658 uncorrected forecast while an additional variability correction (or one-predictor correction)
659 yields 4% of extra reduction. By far the strongest correction (45% extra reduction) derives
660 from the use of the best two-predictor correction. The situation is clearly different for post-
661 processing applied to the analysis where all correction methods pull the analysis away from
662 the observations (increased RMSE).

663 The main second predictor that reduces the RMSE associated with the 5-day *forecast* is
664 model sea-surface temperature (SST). Almost all other (second) predictors that are not
665 directly related to the model SST improve marginally or deteriorate upon the one-predictor
666 forecast. Using the model SST (averaged south of 50°S) as a second predictor to correct
667 the antarctic sea ice area, the RMSE is reduced with 50% as compared to the one-predictor
668 forecast (see Table 3). Correcting the Antarctic sea ice area as a function of longitude using
669 the model SST amounts to a reduction of 12%. This is a strong indication of a model error
670 correlated with SST that considerably affects the forecast of the sea ice area. The global

671 view of the modeling impact on forecasts allows for emphasizing the dominant role played by
672 model errors associated with sea surface temperature forecasts. Improvements will therefore
673 be expected provided a better representation of sea surface temperature is achieved.

674 Fig. 15 shows the average Antarctic sea ice area for the different forecasts, the analysis and
675 the observation as a function of the day of the year and the RMSE associated with these
676 forecasts is given in Fig. 16. Clearly the RMSE of the two-predictor corrected forecast has
677 the weakest seasonal cycle. Analogously, Fig. 17 depicts the longitudinal RMSE dependence
678 of the sea ice area as function of longitude. The strongest two-predictor corrections are
679 obtained in the Ross and Weddell seas and during Antarctic summer.

680 The best two-predictor correction scheme for the analysis leads to a larger value of the
681 RMSE. As discussed in details in [Vannitsem and Nicolis \(2008\)](#), the absence of correction of
682 the post-processing approach indicates that no model errors nor initial biases (related to the
683 observations) are affecting the analyses, or in other words that the sole error present in the
684 analysis is a random initial condition error and that the data assimilation scheme has made
685 a proper use of the observations.

686

687 In turn the presence of a purely random initial condition error affecting the forecast step
688 of the data assimilation scheme allows for concluding that the large biases of the five-day
689 forecast are predominantly induced by a model error strongly correlated to the model SST.
690 Even though so far no specific modeling scheme - such as horizontal turbulent transport - is
691 pinpointed as the source of model error, we believe that progress can be made by considering
692 other predictors more related to some specific parameterization schemes. This question is
693 worth addressing in the future.

694 Once a second predictor providing substantial corrections is found, the variables or parame-
695 terization tendencies that strongly affect this predictor must be used to define more specific
696 predictors for the post-processing scheme. Since, in our case, the model error is strongly
697 correlated with SST, new predictors related to surface heat fluxes, ice melting or freezing, or
698 the parameterization of eddy-induced mixing at sub-grid scales could be good candidates.

699 Once the observables responsible of the model error are isolated, the parameterization scheme
700 should be reassessed, and sensitivity analyses based for instance on adjoint models could be
701 performed.

702 Note that the post-processing approach as proposed here is not equivalent to finding variables
703 that are highly correlated with the observations. In addition the use of different interpolation
704 schemes could affect the amplitude of the absolute RMSE values, but the ratio between
705 the best two-predictor scheme and the one-predictor scheme is not affected, suggesting the
706 robustness of the conclusions.

707 **8. Conclusions**

708 This study shows that sea ice drift can be used to correct the wind field over the Southern
709 Ocean as the model sea ice drift and 3-day mean surface wind field are strongly correlated.
710 This relationship was used to adjust the wind field using pseudo-wind field observations
711 based on sea ice drift data. As expected, the model using the adjusted wind field produces
712 results closer to the sea ice drift data. But the adjusted wind field is also closer to the Cross-
713 Calibrated Multi-Platform Ocean Surface Wind field (based on ERA-40 and observations).
714 The impact on sea ice concentration was also assessed. However, only a small error reduction
715 was found which suggests that only a small part of the model error in sea ice concentration is
716 due to the wind fields. Comparison of the adjusted wind fields with direct wind observations
717 would be useful to further assess the validity of the wind corrections.

718 Based on this adjusted wind, a reanalysis using the global NEMO model ORCA2 for the
719 period 1985 to 2006 using 50 ensemble members has been presented. This model assimilates
720 sea surface temperature, sea ice concentration and sea ice drift. The sea ice concentration
721 assimilation used a Gaussian anamorphosis to transform this variable into a variable which
722 follows more closely a Gaussian distribution. This transformation resulted in an improvement
723 of the sea ice forecast. Despite this improvement being relatively small, the cost in term of
724 CPU time is vanishingly small compared to the ensemble forecast and the analysis.

725 Finally, the reanalysis was compared to the World Ocean Database which is an indepen-
726 dent data set. The assimilation was able to reduce the overall RMS error and bias of the

727 model compared to *in situ* temperature and salinity profiles. As the focus of the reanalysis
728 is the Southern Ocean, the impact of the assimilation on the ACC (Antarctic Circumpolar
729 Current) was also assessed by comparing the mean sea surface height of the model to the
730 mean dynamic topography derived from various observations. The assimilation improved
731 in general the mean surface height of the model in the Southern Ocean. In particular, the
732 overall position and strength of the ACC was closer to observations after the assimilation.

733

734 Data assimilation is not directly suited to correct or diagnose consistent model errors since
735 these are usually considered as random uncorrelated processes (except when the model bias is
736 related to errors in the model parameters which can be estimated using variational assimila-
737 tion or using a Kalman filter with an augmented state vector). The post-processing technique
738 known as model output statistics attempts to relate a series of past forecast variables with
739 the corresponding observations and is commonly used in numerical weather predictions for
740 improving forecasts by reducing the impact of model errors. This technique can also be
741 used to identify the presence of model errors by means of the analysis of the forecast im-
742 provements obtained using multiple predictors (Vannitsem and Nicolis, 2008). Indeed the
743 potential forecast improvement based on a predictor reflects the presence of model errors
744 (systematic or not) strongly correlated with this specific predictor. In the present investiga-
745 tion, the cross-validated RMS error of the 5-day forecast for the total Antarctic sea ice area
746 could be halved using the SST forecast (averaged south of 50°S) as predictor. This indicates
747 that SST is an important predictor strongly affected by the modelling error. This finding
748 constitutes a first step to the identification of the underlying modeling scheme at the origin
749 of the model error affecting the forecast. The post-processing technique was also applied on
750 the analysis but was unable to reduce the RMS error, indicating that there is no obvious
751 systematic error affecting the sea ice analysis.

752 9. Acknowledgments

753 This work was funded by the project [PREDANTAR](#) (SD/CA/04A) from the federal Bel-
754 gian Science policy and the [Sangoma](#) FP7-SPACE-2011 project (grant 283580). François

755 Massonnet is a F.R.S. - FNRS Post-Doctoral Fellow and Alexander Barth a F.R.S. - FNRS
756 Research Associate. NCEP/NCAR Reanalysis data provided by the NOAA/OAR/ESRL
757 PSD, Boulder, Colorado, USA, from their Web site at <http://www.esrl.noaa.gov/psd/>.
758 The UK Met Office, EUMETSAT OSI-SAF and MyOcean are acknowledged for providing
759 the OSTIA/OSI-SAF sea surface temperature and sea ice concentration. We also thank the
760 National Snow and Ice Data Center for providing the ice drift data, the World Ocean Data
761 Base for the in situ temperature and salinity profiles, CNES and CLS for the mean dynamic
762 topography. This is a MARE publication.

763 D. G. Vaughan, J. C. Comiso, I. Allison, J. Carrasco, R. Kwok, P. Mote, T. Murray, F. Paul,
764 J. Ren, E. Rignot, O. Solomina, K. Steffen, T. Zhang, Observations:Cryosphere, in: T. F.
765 Stocker, D. Qin, G.-K. Plattner, M. Tignor, S. K. Allen, J. Boschung, A. Nauels, Y. Xia,
766 V. Bex, P. M. Midgley (Eds.), *Climate Change 2013: The Physical Science Basis. Con-*
767 *tribution of Working Group I to the Fifth Assessment Report of the Intergovernmental*
768 *Panel on Climate Change*, Cambridge University Press, Cambridge, United Kingdom and
769 New York, NY, USA, 2013.

770 I. Eisenman, W. N. Meier, J. R. Norris, A spurious jump in the satellite record: has Antarctic
771 sea ice expansion been overestimated?, *The Cryosphere* 8 (4) (2014) 1289–1296, doi:[10.5194/tc-8-1289-2014](https://doi.org/10.5194/tc-8-1289-2014).
772

773 J. Turner, J. Overland, Contrasting climate change in the two polar regions, *Polar Research*
774 28 (2) (2009) 146–164, ISSN 1751-8369, doi:[10.1111/j.1751-8369.2009.00128.x](https://doi.org/10.1111/j.1751-8369.2009.00128.x).

775 S. Solomon, Stratospheric ozone depletion: A review of concepts and history, *Rev. Geophys.*
776 37 (3) (1999) 275–316, doi:[10.1029/1999RG900008](https://doi.org/10.1029/1999RG900008).

777 C. M. Bitz, L. M. Polvani, Antarctic climate response to stratospheric ozone depletion
778 in a fine resolution ocean climate model, *Geophys. Res. Lett.* 39 (20), doi:[10.1029/2012GL053393](https://doi.org/10.1029/2012GL053393).
779

780 K. L. Smith, L. M. Polvani, D. R. Marsh, Mitigation of 21st century Antarctic sea ice loss
781 by stratospheric ozone recovery, *Geophys. Res. Lett.* 39 (20), doi:[10.1029/2012GL053325](https://doi.org/10.1029/2012GL053325).

782 M. Sigmond, J. C. Fyfe, The Antarctic Sea Ice Response to the Ozone Hole in Climate
783 Models, *Journal of Climate* 27 (3) (2013) 1336–1342, doi:[10.1175/JCLI-D-13-00590.1](https://doi.org/10.1175/JCLI-D-13-00590.1).

784 J. Zhang, Increasing Antarctic Sea Ice under Warming Atmospheric and Oceanic Conditions,
785 *Journal of Climate* 20 (2007) 2515–2529, doi:[10.1175/JCLI4136.1](https://doi.org/10.1175/JCLI4136.1).

786 S. E. Stammerjohn, D. G. Martinson, R. C. Smith, X. Yuan, D. Rind, Trends in Antarctic
787 annual sea ice retreat and advance and their relation to El Niño Southern Oscillation and
788 Southern Annular Mode variability, *J. Geophys. Res.* 113 (C3), doi:[10.1029/2007JC004269](https://doi.org/10.1029/2007JC004269).

789 H. Goosse, W. Lefebvre, A. de Montety, E. Cresspin, A. Orsi, Consistent past half-century
790 trends in the atmosphere, the sea ice and the ocean at high southern latitudes, *Climate*
791 *Dynamics* 33 (7) (2009) 999–1016–1016, doi:[10.1007/s00382-008-0500-9](https://doi.org/10.1007/s00382-008-0500-9).

792 C. H. Kirkman, C. M. Bitz, The Effect of the Sea Ice Freshwater Flux on Southern Ocean
793 Temperatures in CCSM3: Deep-Ocean Warming and Delayed Surface Warming, *Journal*
794 *of Climate* 24 (9) (2011) 2224–2237, doi:[10.1175/2010JCLI3625.1](https://doi.org/10.1175/2010JCLI3625.1).

795 L. Landrum, M. M. Holland, D. P. Schneider, E. Hunke, Antarctic Sea Ice Climatology,
796 Variability, and Late Twentieth-Century Change in CCSM4, *Journal of Climate* 25 (14)
797 (2012) 4817–4838, doi:[10.1175/JCLI-D-11-00289.1](https://doi.org/10.1175/JCLI-D-11-00289.1).

798 P. R. Holland, R. Kwok, Wind-driven trends in Antarctic sea-ice drift, *Nature Geoscience* 5
799 (2012) 872–875, doi:[10.1038/ngeo1627](https://doi.org/10.1038/ngeo1627).

800 R. Bintanja, G. J. van Oldenborgh, S. S. Drijfhout, B. Wouters, C. A. Katsman, Important
801 role for ocean warming and increased ice-shelf melt in Antarctic sea-ice expansion, *Nature*
802 *Geoscience* 6 (5) (2013) 376–379, doi:[10.1038/ngeo1767](https://doi.org/10.1038/ngeo1767).

803 H. Goosse, V. Zunz, Decadal trends in the Antarctic sea ice extent ultimately controlled by
804 ice–ocean feedback, *The Cryosphere* 8 (2) (2014) 453–470, doi:[10.5194/tc-8-453-2014](https://doi.org/10.5194/tc-8-453-2014).

- 805 C. de Lavergne, J. B. Palter, E. D. Galbraith, R. Bernardello, I. Marinov, Cessation of deep
806 convection in the open Southern Ocean under anthropogenic climate change, *Nature Clim.*
807 *Change* 4 (4) (2014) 278–282, doi:[10.1038/nclimate2132](https://doi.org/10.1038/nclimate2132).
- 808 I. Mahlstein, P. R. Gent, S. Solomon, Historical Antarctic mean sea ice area, sea ice trends,
809 and winds in CMIP5 simulations, *Journal of Geophysical Research: Atmospheres* 118
810 (2013) 1–6, ISSN 2169-8996, doi:[10.1002/jgrd.50443](https://doi.org/10.1002/jgrd.50443).
- 811 V. Zunz, H. Goosse, F. Massonnet, How does internal variability influence the ability of
812 CMIP5 models to reproduce the recent trend in Southern Ocean sea ice extent?, *The*
813 *Cryosphere* 7 (2) (2013) 451–468, doi:[10.5194/tc-7-451-2013](https://doi.org/10.5194/tc-7-451-2013).
- 814 L. M. Polvani, K. L. Smith, Can natural variability explain observed Antarctic sea ice trends?
815 New modeling evidence from CMIP5, *Geophys. Res. Lett.* 40 (12) (2013) 3195–3199, ISSN
816 1944-8007, doi:[10.1002/grl.50578](https://doi.org/10.1002/grl.50578).
- 817 N. C. Swart, J. C. Fyfe, The influence of recent Antarctic ice sheet retreat on simulated sea ice
818 area trends, *Geophysical Research Letters* 40 (16) (2013) 4328–4332, doi:[10.1002/grl.5082](https://doi.org/10.1002/grl.5082).
- 819 C. L. Parkinson, D. J. Cavalieri, Antarctic sea ice variability and trends, 1979–2010, *The*
820 *Cryosphere* 6 (4) (2012) 871–880, ISSN 1994-0424, doi:[10.5194/tc-6-871-2012](https://doi.org/10.5194/tc-6-871-2012).
- 821 K. E. Taylor, R. J. Stouffer, G. A. Meehl, An Overview of CMIP5 and the Experiment
822 Design, *Bulletin of the American Meteorological Society* 93 (4) (2011) 485–498, doi:[10.1175/BAMS-D-11-00094.1](https://doi.org/10.1175/BAMS-D-11-00094.1).
- 823
- 824 J. Turner, T. J. Bracegirdle, T. Phillips, G. J. Marshall, J. S. Hosking, An Initial Assessment
825 of Antarctic Sea Ice Extent in the CMIP5 Models, *Journal of Climate* 26 (5) (2013) 1473–
826 1484, doi:[10.1175/JCLI-D-12-00068.1](https://doi.org/10.1175/JCLI-D-12-00068.1).
- 827 T. Fichefet, M. A. Morales Maqueda, Modelling the influence of snow accumulation and
828 snow-ice formation on the seasonal cycle of the Antarctic sea-ice cover, *Climate Dynamics*
829 15 (1999) 251–268, doi:[10.1007/s003820050280](https://doi.org/10.1007/s003820050280).

- 830 T. Fichefet, H. Goosse, M. A. Morales Maqueda, A hindcast simulation of Arctic and Antarc-
831 tic sea ice variability, 1955–2001, *Polar Research* 22 (2003) 91–98, doi:[10.1111/j.1751-8369.
832 2003.tb00100.x](https://doi.org/10.1111/j.1751-8369.2003.tb00100.x).
- 833 P. R. Holland, N. Bruneau, C. Enright, M. Losch, N. T. Kurtz, R. Kwok, Modeled Trends
834 in Antarctic Sea Ice Thickness, *J. Climate* 27 (10) (2014) 3784–3801, ISSN 0894-8755,
835 doi:[10.1175/JCLI-D-13-00301.1](https://doi.org/10.1175/JCLI-D-13-00301.1).
- 836 D. H. Bromwich, R. L. Fogt, K. I. Hodges, J. E. Walsh, A tropospheric assessment of the
837 ERA-40, NCEP, and JRA-25 global reanalyses in the polar regions, *Journal of Geophysical*
838 *Research* 112 (2007) D10111, doi:[10.1029/2006JD007859](https://doi.org/10.1029/2006JD007859).
- 839 K. Hines, D. H. Bromwich, G. J. Marshall, Artificial Surface Pressure Trends in the
840 NCEP/NCAR Reanalysis over the Southern Ocean and Antarctica, *Journal of Climate* 13
841 (2000) 3940–3952, doi:[10.1175/1520-0442\(2000\)013<3940:ASPTIT>2.0.CO;2](https://doi.org/10.1175/1520-0442(2000)013<3940:ASPTIT>2.0.CO;2).
- 842 M. Vancoppenolle, R. Timmermann, S. F. Ackley, T. Fichefet, H. Goosse, P. Heil, K. C.
843 Leonard, J. Lieser, M. Nicolaus, T. Papakyriakou, J.-L. Tison, Assessment of radiation
844 forcing data sets for large-scale sea ice models in the Southern Ocean, *Deep Sea Research*
845 *Part II: Topical Studies in Oceanography* 58 (2011) 1237–1249, ISSN 0967-0645, doi:[10.
846 1016/j.dsr2.2010.10.039](https://doi.org/10.1016/j.dsr2.2010.10.039).
- 847 R. Timmerman, A. P. Worby, H. Goosse, T. Fichefet, Utilizing the ASPeCt sea ice thickness
848 data set to evaluate a global coupled sea ice–ocean model, *Journal of Geophysical Research*
849 109 (2004) C07017, doi:[10.1029/2003JC002242](https://doi.org/10.1029/2003JC002242).
- 850 A. Stössel, Z. Zhang, T. Vihma, The effect of alternative real-time wind forcing on Southern
851 Ocean sea ice simulations, *Journal of Geophysical Research* 116 (2011) C11021, doi:[10.
852 1029/2011JC007328](https://doi.org/10.1029/2011JC007328).
- 853 D. Stammer, C. Wunsch, R. Giering, C. Eckert, P. Heimbach, J. Marotzke, A. Adcroft,
854 C. N. Hill, J. Marshall, Global ocean circulation during 1992–1997, estimated from ocean

855 observations and a general circulation model, *J.-Geophys.-Res.* 107 (C9) (2002) 3118, ISSN
856 2156-2202, doi:[10.1029/2001JC000888](https://doi.org/10.1029/2001JC000888).

857 A. Stössel, Employing Satellite-Derived Sea Ice Concentration to Constrain Upper-Ocean
858 Temperature in a Global Ocean GCM, *J. Climate* 21 (17) (2008) 4498–4513, ISSN 0894-
859 8755, doi:[10.1175/2008JCLI2256.1](https://doi.org/10.1175/2008JCLI2256.1).

860 F. Massonnet, P. Mathiot, T. Fichefet, H. Goosse, C. K. Beatty, M. Vancoppenolle,
861 T. Lavergne, A model reconstruction of the Antarctic sea ice thickness and volume changes
862 over 1980-2008 using data assimilation, *Ocean Modelling* 64 (2013) 67–75, ISSN 1463-5003,
863 doi:[10.1016/j.ocemod.2013.01.003](https://doi.org/10.1016/j.ocemod.2013.01.003).

864 N. Ferry, L. Parent, G. Garric, C. Bricaud, C. E. Testut, O. Le Galloudec, J.-M. Lellouche,
865 M. Drévillon, E. Greiner, B. Barnier, J. M. Molines, N. Jourdain, S. Guinehut, C. Cabanes,
866 L. Zawadski, GLORYS2V1 Global ocean reanalysis of the altimetric era (1993-2009) at
867 meso scale, Tech. Rep., Mercator Ocean, 2012.

868 M. A. Balmaseda, A. Vidard, D. L. T. Anderson, The ECMWF Ocean Analysis Sys-
869 tem: ORA-S3, *Mon. Wea. Rev.* 136 (8) (2008) 3018–3034, ISSN 0027-0644, doi:[10.1175/
870 2008MWR2433.1](https://doi.org/10.1175/2008MWR2433.1).

871 J. A. Carton, B. S. Giese, A Reanalysis of Ocean Climate Using Simple Ocean Data As-
872 similation (SODA), *Mon. Wea. Rev.* 136 (8) (2008) 2999–3017, ISSN 0027-0644, doi:
873 [10.1175/2007MWR1978.1](https://doi.org/10.1175/2007MWR1978.1).

874 T. Janjić, J. Schröter, R. Savcenko, W. Bosch, A. Albertella, R. Rummel, O. Klatt, Impact of
875 combining GRACE and GOCE gravity data on ocean circulation estimates, *Ocean Science*
876 8 (1) (2012) 65–79, doi:[10.5194/os-8-65-2012](https://doi.org/10.5194/os-8-65-2012).

877 P. Sakov, F. Counillon, L. Bertino, K. A. Lisæter, P. R. Oke, A. Korablev, TOPAZ4: an
878 ocean-sea ice data assimilation system for the North Atlantic and Arctic, *Ocean Science*
879 8 (4) (2012) 633–656, doi:[10.5194/os-8-633-2012](https://doi.org/10.5194/os-8-633-2012).

- 880 P. Mathiot, C. König Beatty, T. Fichefet, H. Goosse, F. Massonnet, M. Vancoppenolle, Better
881 constraints on the sea-ice state using global sea-ice data assimilation, *Geosci. Model Dev.*
882 5 (6) (2012) 1501–1515, ISSN 1991-9603, doi:[10.5194/gmd-5-1501-2012](https://doi.org/10.5194/gmd-5-1501-2012).
- 883 L. Bertino, G. Evensen, H. Wackernagel, Sequential Data Assimilation Techniques
884 in Oceanography, *International Statistical Review* 71 (2003) 223–241, doi:[10.1111/j.
885 1751-5823.2003.tb00194.x](https://doi.org/10.1111/j.1751-5823.2003.tb00194.x).
- 886 E. Simon, L. Bertino, Application of the Gaussian anamorphosis to assimilation in a 3-D cou-
887 pled physical-ecosystem model of the North Atlantic with the EnKF: a twin experiment,
888 *Ocean Science* 5 (4) (2009) 495–510, doi:[10.5194/os-5-495-2009](https://doi.org/10.5194/os-5-495-2009).
- 889 D. Béal, P. Brasseur, J.-M. Brankart, Y. Ourmières, J. Verron, Characterization of mixing
890 errors in a coupled physical biogeochemical model of the North Atlantic: implications
891 for nonlinear estimation using Gaussian anamorphosis, *Ocean Science* 6 (2010) 247–262,
892 doi:[10.5194/os-6-247-2010](https://doi.org/10.5194/os-6-247-2010).
- 893 K. A. Lisæter, J. Rosanova, G. Evensen, Assimilation of ice concentration in a coupled
894 ice-ocean model, using the Ensemble Kalman filter, *Ocean Dynamics* 53 (2003) 368–388,
895 doi:[10.1007/s10236-003-0049-4](https://doi.org/10.1007/s10236-003-0049-4).
- 896 F. Massonnet, H. Goosse, T. Fichefet, F. Counillon, Calibration of sea ice dynamic parame-
897 ters in an ocean-sea ice model using an ensemble Kalman filter, *J. Geophys. Res. Oceans*
898 119 (7) (2014) 4168–4184, ISSN 2169-9291, doi:[10.1002/2013JC009705](https://doi.org/10.1002/2013JC009705).
- 899 A. Barth, A. Alvera-Azcárate, J.-M. Beckers, J. Staneva, E. V. Stanev, J. Schulz-Stellenfleth,
900 Correcting surface winds by assimilating High-Frequency Radar surface currents in the
901 German Bight, *Ocean Dynamics* 61 (5) (2011) 599–610, doi:[10.1007/s10236-010-0369-0](https://doi.org/10.1007/s10236-010-0369-0),
902 URL <http://hdl.handle.net/2268/83330>.
- 903 J. Marmain, A. Molcard, P. Forget, A. Barth, Y. Ourmières, Assimilation of HF radar surface
904 currents to optimize forcing in the northwestern Mediterranean Sea, *Nonlinear Processes*
905 *Geophysics* 21 (2014) 659–675, doi:[10.5194/npg-21-659-2014](https://doi.org/10.5194/npg-21-659-2014).

- 906 H. Ngodock, M. Carrier, A 4DVAR System for the Navy Coastal Ocean Model. Part I:
907 System Description and Assimilation of Synthetic Observations in Monterey Bay, Mon.
908 Wea. Rev. 142 (6) (2014) 2085–2107, ISSN 0027-0644, doi:[10.1175/MWR-D-13-00221.1](https://doi.org/10.1175/MWR-D-13-00221.1).
- 909 N. Kimura, Sea ice motion in response to surface wind and ocean current in the Southern
910 Ocean, Journal of the Meteorological Society of Japan 82 (2004) 1223–1231, doi:[10.2151/
911 jmsj.2004.1223](https://doi.org/10.2151/jmsj.2004.1223).
- 912 P. Malanotte-Rizzoli, R. E. Young, D. B. Haidvogel, Initialization and data assimilation
913 experiments with a primitive equation model, Dynamics of Atmospheres and Oceans 13
914 (1989) 349–378, doi:[10.1016/0377-0265\(89\)90046-8](https://doi.org/10.1016/0377-0265(89)90046-8).
- 915 A. Barth, J.-M. Beckers, A. Alvera-Azcárate, R. H. Weisberg, Filtering inertia-gravity waves
916 from the initial conditions of the linear shallow water equations, Ocean Modelling 19 (2007)
917 204–218, doi:[10.1016/j.ocemod.2007.06.007](https://doi.org/10.1016/j.ocemod.2007.06.007), URL <http://hdl.handle.net/2268/4266>.
- 918 Y. Yan, A. Barth, J. Beckers, Comparison of different assimilation schemes in a sequential
919 Kalman filter assimilation system, Ocean Modelling 73 (0) (2014) 123–137, ISSN 1463-
920 5003, doi:[10.1016/j.ocemod.2013.11.002](https://doi.org/10.1016/j.ocemod.2013.11.002), URL <http://hdl.handle.net/2268/163077>.
- 921 G. Madec, NEMO ocean engine, no. 27 in Note du Pole de modélisation, Institut Pierre-
922 Simon Laplace (IPSL), France, 2008.
- 923 T. Fichefet, M. A. Morales Maqueda, Sensitivity of a global sea ice model to the treatment
924 of ice thermodynamics and dynamics, Journal of Geophysical Research 102 (1997) 12609–
925 12646, doi:[10.1029/97JC00480](https://doi.org/10.1029/97JC00480).
- 926 R. Timmermann, H. Goosse, G. Madec, T. Fichefet, C. Etche, V. Dulière, On the represen-
927 tation of high latitude processes in the ORCA-LIM global coupled sea ice-ocean model,
928 Ocean Modelling 8 (1-2) (2005) 175–201, ISSN 1463-5003, doi:[10.1016/j.ocemod.2003.12.
929 009](https://doi.org/10.1016/j.ocemod.2003.12.009).

- 930 S. Bouillon, M. A. Morales Maqueda, V. Legat, T. Fichefet, An elastic-viscous-plastic sea
931 ice model formulated on Arakawa B and C grids, *Ocean Modelling* 27 (2009) 174–184,
932 doi:[10.1016/j.ocemod.2009.01.004](https://doi.org/10.1016/j.ocemod.2009.01.004).
- 933 P. Mathiot, H. Goosse, T. Fichefet, B. Barnier, H. Gallée, Modelling the seasonal vari-
934 ability of the Antarctic Slope Current, *Ocean Science* 7 (4) (2011) 455–470, doi:[10.5194/
935 os-7-455-2011](https://doi.org/10.5194/os-7-455-2011).
- 936 E. Kalnay, M. Kanamitsu, R. Kistler, W. Collins, D. Deaven, L. Gandin, M. Iredell, S. Saha,
937 G. White, J. Woollen, Y. Zhu, A. Leetmaa, R. Reynolds, M. Chelliah, W. Ebisuzaki,
938 W. Higgins, J. Janowiak, K. C. Mo, C. Ropelewski, J. Wang, R. Jenne, D. Joseph, The
939 NCEP/NCAR 40-Year Reanalysis Project, *Bulletin of the American Meteorological Soci-*
940 *ety* 77 (1996) 437–471, doi:[10.1175/1520-0477\(1996\)077<0437:TNYRP>2.0.CO;2](https://doi.org/10.1175/1520-0477(1996)077<0437:TNYRP>2.0.CO;2).
- 941 H. Goosse, T. Fichefet, Importance of ice-ocean interactions for the global ocean circulation:
942 A model study, *Journal of Geophysical Research* 104 (C10) (1999) 23337–23355, ISSN
943 2156-2202, doi:[10.1029/1999JC900215](https://doi.org/10.1029/1999JC900215).
- 944 J. Roberts-Jones, E. K. Fiedler, M. J. Martin, Daily, Global, High-Resolution SST and Sea
945 Ice Reanalysis for 1985-2007 Using the OSTIA System, *J. Climate* 25 (2012) 6215–6232,
946 doi:[10.1175/JCLI-D-11-00648.1](https://doi.org/10.1175/JCLI-D-11-00648.1).
- 947 C. Fowler, Polar Pathfinder Daily 25 km EASE-Grid Sea Ice Motion Vectors, Tech. Rep.,
948 NASA DAAC at the National Snow and Ice Data Center, Boulder, Colorado USA, 2003.
- 949 P. K. Kundu, J. S. Allen, Some three-dimensional characteristics of low-frequency current
950 fluctuations near the Oregon coast, *Journal of Physical Oceanography* 6 (1976) 181–199,
951 doi:[10.1175/1520-0485\(1976\)006<0181:STDCOL>2.0.CO;2](https://doi.org/10.1175/1520-0485(1976)006<0181:STDCOL>2.0.CO;2).
- 952 A. Alvera-Azcárate, A. Barth, D. Sirjacobs, J.-M. Beckers, Enhancing temporal correlations
953 in EOF expansions for the reconstruction of missing data using DINEOF, *Ocean Science*
954 5 (2009) 475–485, doi:[10.5194/os-5-475-2009](https://doi.org/10.5194/os-5-475-2009), URL [http://www.ocean-sci.net/5/475/
955 2009/](http://www.ocean-sci.net/5/475/2009/).

- 956 A. Barth, A. Alvera-Azcárate, R. H. Weisberg, Assimilation of high-frequency radar currents
957 in a nested model of the West Florida Shelf, *Journal of Geophysical Research* 113 (2008)
958 C08033, doi:[10.1029/2007JC004585](https://doi.org/10.1029/2007JC004585), URL <http://hdl.handle.net/2268/26171>.
- 959 R. Atlas, R. N. Hoffman, J. Ardizzone, S. M. Leidner, J. C. Jusem, D. K. Smith, D. Gombos,
960 A cross-calibrated, multiplatform ocean surface wind velocity product for meteorological
961 and oceanographic applications, *Bulletin of the American Meteorological Society* 92 (2011)
962 157–174, doi:[10.1175/2010BAMS2946.1](https://doi.org/10.1175/2010BAMS2946.1).
- 963 A. Barth, J.-M. Beckers, C. Troupin, A. Alvera-Azcárate, L. Vandenbulcke, divand-
964 1.0: n-dimensional variational data analysis for ocean observations, *Geoscientific Model*
965 *Development* 7 (1) (2014) 225–241, doi:[10.5194/gmd-7-225-2014](https://doi.org/10.5194/gmd-7-225-2014), URL [http://www.
966 geosci-model-dev.net/7/225/2014/](http://www.geosci-model-dev.net/7/225/2014/).
- 967 P. Brasseur, J.-M. Beckers, J.-M. Brankart, R. Schoenauen, Seasonal Temperature and Salin-
968 ity Fields in the Mediterranean Sea: Climatological Analyses of an Historical Data Set.,
969 *Deep-Sea Research* 43 (2) (1996) 159–192, doi:[10.1016/0967-0637\(96\)00012-X](https://doi.org/10.1016/0967-0637(96)00012-X).
- 970 P. Mathiot, B. Barnier, H. Gallée, J. M. Molines, J. L. Sommer, M. Juza, T. Penduff,
971 Introducing katabatic winds in global ERA40 fields to simulate their impacts on the
972 Southern Ocean and sea-ice, *Ocean Modelling* 35 (3) (2010) 146 – 160, ISSN 1463-5003,
973 doi:[10.1016/j.ocemod.2010.07.001](https://doi.org/10.1016/j.ocemod.2010.07.001).
- 974 R. Massom, P. Harris, K. Michael, M. Potter, The distribution and formative processes of
975 latent-heat polynyas in East Antarctica, *Annals of Glaciology* 27 (1998) 420–426.
- 976 M. A. Morales Maqueda, A. J. Willmott, N. R. T. Biggs, Polynya Dynamics: a Review of
977 Observations and Modeling, *Reviews of Geophysics* 42 (1) (2004) RG1004, ISSN 1944-
978 9208, doi:[10.1029/2002RG000116](https://doi.org/10.1029/2002RG000116).
- 979 H. Sumata, T. Lavergne, F. Girard-Ardhuin, N. Kimura, M. A. Tschudi, F. Kauker,
980 M. Karcher, R. Gerdes, An intercomparison of Arctic ice drift products to deduce un-

- 981 certainty estimates, *Journal of Geophysical Research: Oceans* 119 (8) (2014) 4887–4921,
982 ISSN 2169-9291, doi:[10.1002/2013JC009724](https://doi.org/10.1002/2013JC009724).
- 983 C. H. Bishop, B. Etherton, S. J. Majumdar, Adaptive Sampling with the Ensemble Trans-
984 form Kalman Filter. Part I: Theoretical Aspects, *Monthly Weather Review* 129 (2001)
985 420–436, doi:[10.1175/1520-0493\(2001\)129<0420:ASWTET>2.0.CO;2](https://doi.org/10.1175/1520-0493(2001)129<0420:ASWTET>2.0.CO;2).
- 986 L. Vandenbulcke, M. Rixen, J.-M. Beckers, A. Alvera-Azcárate, A. Barth, An analysis of the
987 error space of a high-resolution implementation of the GHER hydrodynamic model in the
988 Mediterranean Sea, *Ocean Modelling* 24 (1-2) (2008) 46–64, doi:[10.1016/j.ocemod.2008.](https://doi.org/10.1016/j.ocemod.2008.05.007)
989 [05.007](https://doi.org/10.1016/j.ocemod.2008.05.007), URL <http://hdl.handle.net/2268/4263>.
- 990 F. Lenartz, C. Raick, K. Soetaert, M. Gregoire, Application of an Ensemble Kalman filter
991 to a 1-D coupled hydrodynamicecosystem model of the Ligurian Sea, *Journal of Marine*
992 *Systems* 68 (2007) 327–348, doi:[10.1016/j.jmarsys.2006.12.001](https://doi.org/10.1016/j.jmarsys.2006.12.001).
- 993 Y. Chen, C. Snyder, Assimilating Vortex Position with an Ensemble Kalman Filter, *Monthly*
994 *Weather Review* 135 (2007) 1828–1845, doi:[10.1175/MWR3351.1](https://doi.org/10.1175/MWR3351.1).
- 995 G. Evensen, *Data assimilation: the Ensemble Kalman Filter*, Springer, 279pp, 2007.
- 996 G. H. Golub, C. F. Van Loan, *Matrix Computations*, Johns Hopkins University Press, Bal-
997 timore, 3rd ed. edn., 1996.
- 998 L. Vandenbulcke, A. Barth, M. Rixen, A. Alvera-Azcárate, Z. B. Bouallegue, J.-M. Beck-
999 ers, Study of the combined effects of data assimilation and grid nesting in ocean
1000 models. Application to the Gulf of Lions., *Ocean Science* 2 (2) (2006) 213–222, doi:
1001 [10.5194/os-2-213-2006](https://doi.org/10.5194/os-2-213-2006).
- 1002 A. Alvera-Azcárate, A. Barth, Z. B. Bouallègue, M. Rixen, J.-M. Beckers, Forecast Verifi-
1003 cation of a 3D model of the Ligurian Sea. The use of Discrete Wavelet Transforms in the
1004 skill assessment of spatial forecasts, *Journal of Marine Systems* 65 (1–4) (2007) 460–483,
1005 doi:[10.1016/j.jmarsys.2005.09.015](https://doi.org/10.1016/j.jmarsys.2005.09.015), URL <http://hdl.handle.net/2268/4264>.

- 1006 S. C. Bloom, L. L. Takacs, A. M. D. Silva, D. Ledvina, Data assimilation using incre-
1007 mental analysis updates, *Monthly Weather Review* 124 (1996) 1256–1271, doi:[10.1175/
1008 1520-0493\(1996\)124<1256:DAUIAU>2.0.CO;2](https://doi.org/10.1175/1520-0493(1996)124<1256:DAUIAU>2.0.CO;2).
- 1009 M. H. Rio, S. Guinehut, G. Larnicol, New CNES-CLS09 global mean dynamic topography
1010 computed from the combination of GRACE data, altimetry, and in situ measurements,
1011 *Journal of Geophysical Research: Oceans* 116 (C7) (2011) C07018, ISSN 2156-2202, doi:
1012 [10.1029/2010JC006505](https://doi.org/10.1029/2010JC006505).
- 1013 S. T. Gille, Mean sea surface height of the Antarctic Circumpolar Current from Geosat
1014 data: Method and application, *Journal of Geophysical Research: Oceans* 99 (C9) (1994)
1015 18255–18273, ISSN 2156-2202, doi:[10.1029/94JC01172](https://doi.org/10.1029/94JC01172).
- 1016 E. Klinker, P. Sardeshmukh, The diagnosis of mechanical dissipation in the atmosphere
1017 from large-scale balance requirements, *Journal of the atmospheric sciences* 49 (7) (1992)
1018 608–627, doi:[10.1175/1520-0469\(1992\)049<0608:TDOMDI>2.0.CO;2](https://doi.org/10.1175/1520-0469(1992)049<0608:TDOMDI>2.0.CO;2).
- 1019 S. Schubert, Y. Chang, An objective method for inferring sources of model error, *Monthly*
1020 *Weather Review* 124 (2) (1996) 325–340, doi:[10.1175/1520-0493\(1996\)124<0325:AOMFIS>
1021 2.0.CO;2](https://doi.org/10.1175/1520-0493(1996)124<0325:AOMFIS>2.0.CO;2).
- 1022 M. Rodwell, T. Palmer, Using numerical weather prediction to assess climate models,
1023 *Quarterly Journal of the Royal Meteorological Society* 133 (622) (2007) 129–146, doi:
1024 [10.1002/qj.23](https://doi.org/10.1002/qj.23).
- 1025 S. Vannitsem, C. Nicolis, Dynamical properties of model output statistics forecasts, *Monthly*
1026 *Weather Review* 136 (2) (2008) 405–419, doi:[10.1175/2007MWR2104.1](https://doi.org/10.1175/2007MWR2104.1).
- 1027 F. Di Giuseppe, F. Molteni, A. M. Tompkins, A rainfall calibration methodology for impacts
1028 modelling based on spatial mapping, *Quarterly Journal of the Royal Meteorological Society*
1029 139 (674) (2013) 1389–1401, doi:[10.1002/qj.2019](https://doi.org/10.1002/qj.2019).

Table 1: Calibration of the assimilation configuration. A dash means no significant change.

RMS	state vec.	anam.	$\sqrt{\mathbf{R}_{ice}}$	SST	ice conc.	ui_ice	vi_ice
baseline experiment	full	yes	0.1	0.632	0.087	0.080	0.070
skill score (%)				SST	ice conc.	ui_ice	vi_ice
ExpFNA-0.1	full	no	0.1	-	-2.766	-	-
ExpFA-0.07	full	yes	0.07	-2.556	8.094	-	2.254
ExpRA-0.05	reduced	yes	0.05	-7.477	12.492	4.000	3.069
ExpRA-0.07	reduced	yes	0.07	-2.794	10.046	2.390	2.474
ExpRA-0.1	reduced	yes	0.1	-	13.454	-	2.279

Table 2: Total RMS error relative to assimilated data

	Free	Forecast	Analysis
SST [°C]	0.98	0.59	0.47
ice conc.	0.22	0.085	0.033
u_{ice} [m/s]	0.088	0.069	0.041
v_{ice} [m/s]	0.074	0.060	0.039

Table 3: Root Mean Squared Error (RMSE) of the Antarctic sea ice area of different correction methods applied on the 5-day forecasts (second column) and analysis (third column), all divided by the RMSE of the uncorrected 5-day forecast for Antarctic sea ice area.

Antarctic sea ice area	Forecast RMSE (%)	Analysis RMSE (%)
Uncorrected	100%	15.7%
Bias-corrected	95%	17.2%
One-predictor corrected	91%	18.2%
Two-predictor corrected (min. RMSE)	46%	16.6%

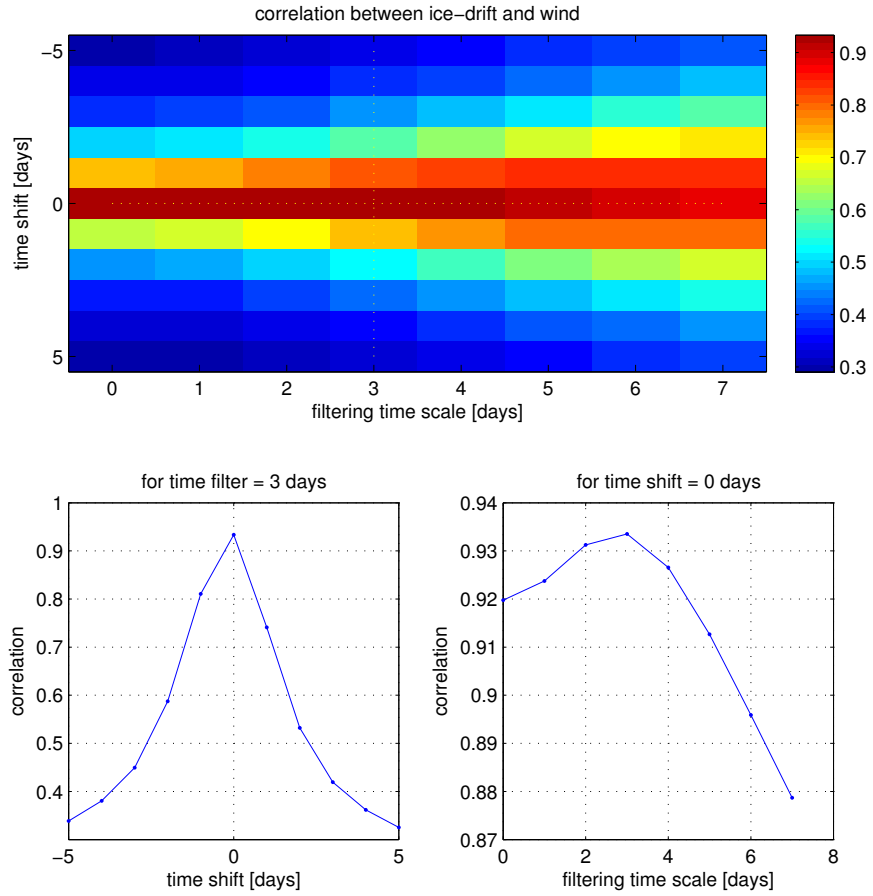


Figure 1: Magnitude of correlation coefficient (for the year 2000) as function of time shift and filtering time scale (panel a). Panel b show the magnitude of correlation coefficient as a function of the time shift for a filtering time scale sets to 3 days (vertical dotted line in panel a) and panel c show represents the magnitude of correlation coefficient as a function of filtering time scale for a the time shift set to 0 days (horizontal dotted line in panel a).

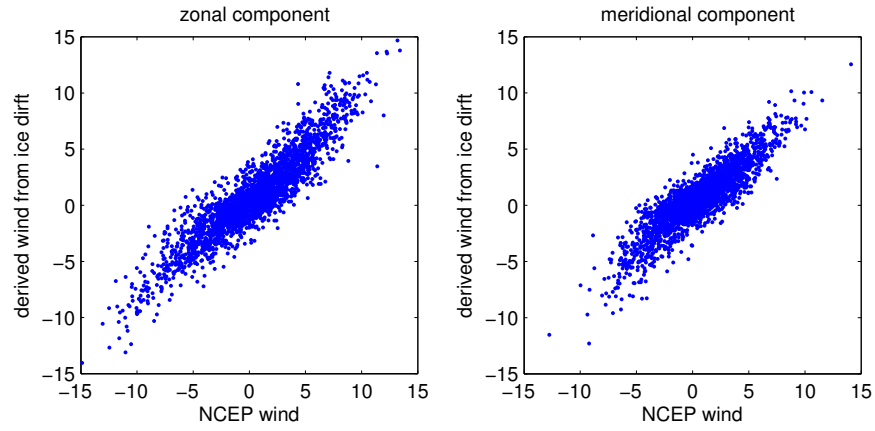


Figure 2: Scatter plot of NCEP wind versus wind estimated from ice drift (both in m/s) using the complex regression coefficient (with a filter of 3 days and without timeshift). The dots corresponds to the data from the year 2000 and to model grid points covered by ice in the Southern Hemisphere.

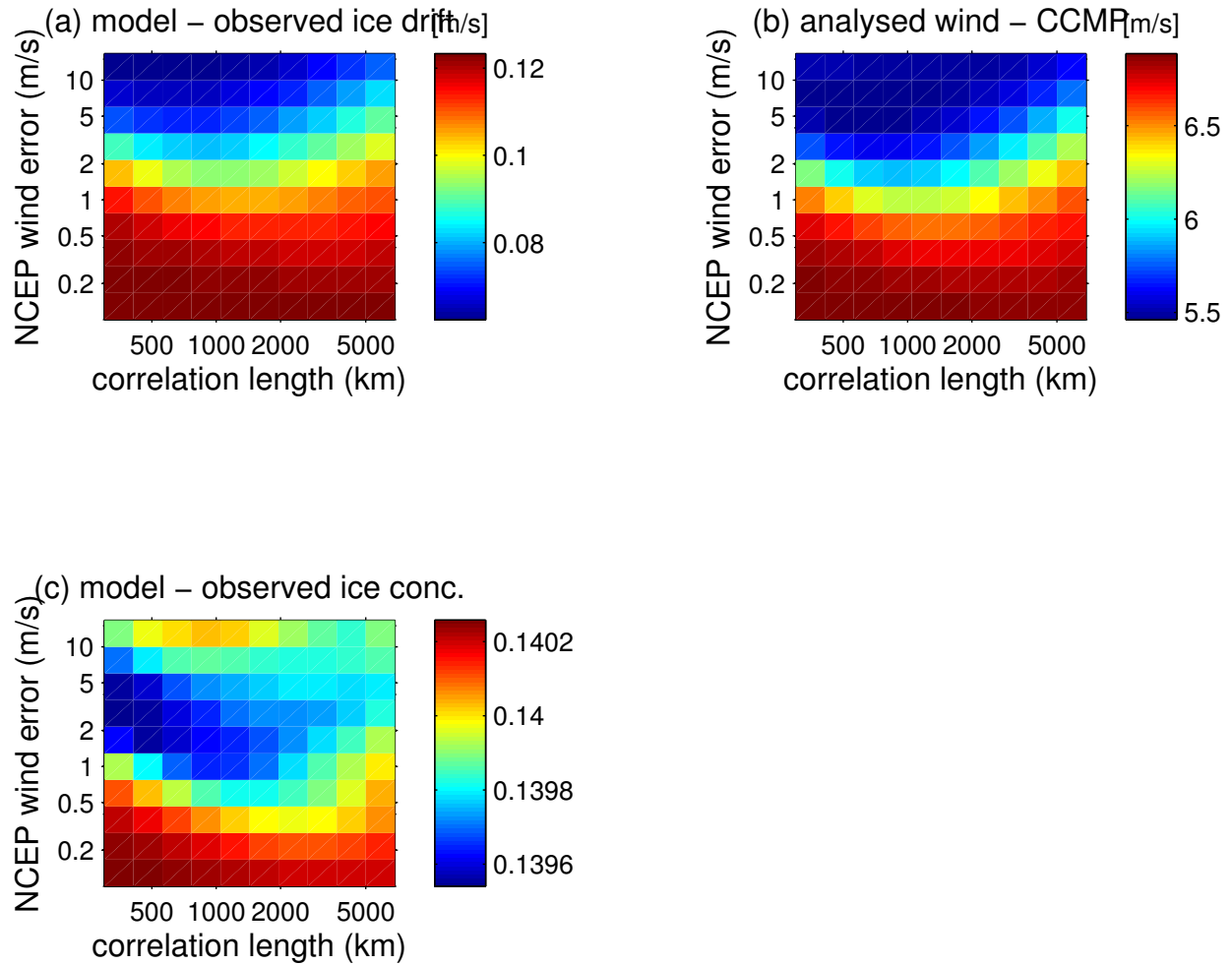


Figure 3: RMS difference of the model and observed sea ice drift (panel a), the analyzed winds and CCMP winds (panel b) and model and observed sea ice concentration (panel c) for different values of the correlation length and the NCEP wind error.

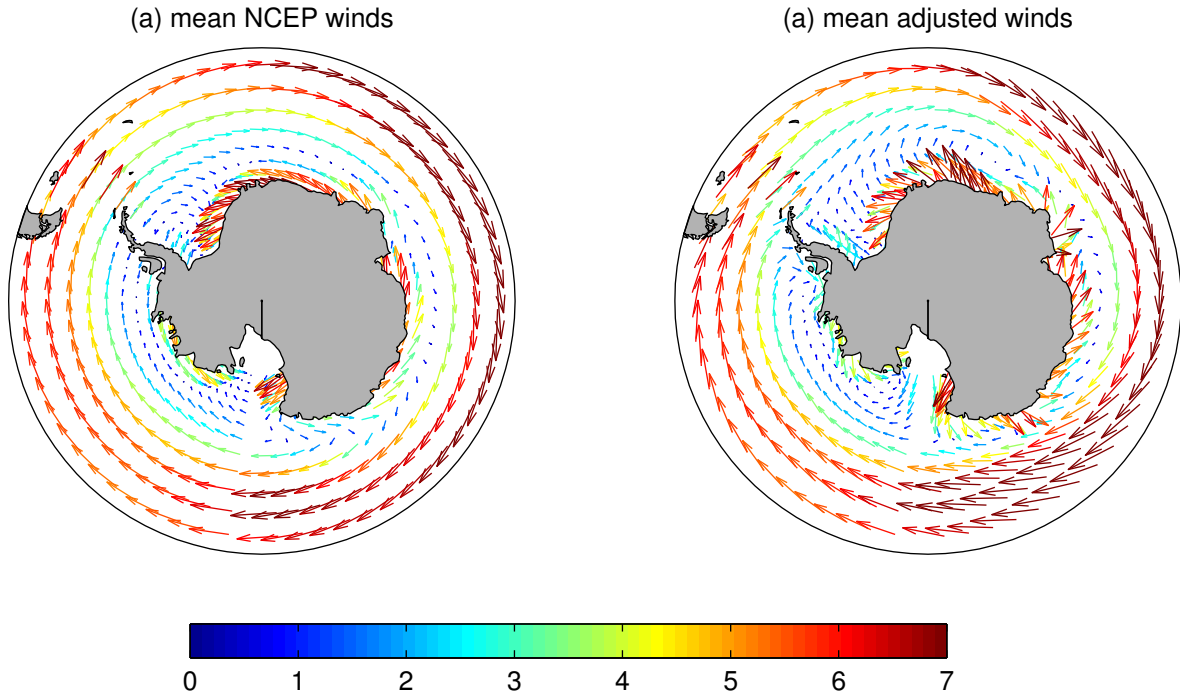


Figure 4: The mean NCEP wind vector (panel a) and the mean adjusted wind (panel b) averaged over the period from 1985 to 2006. The color represents the norm of the wind vector in m/s.

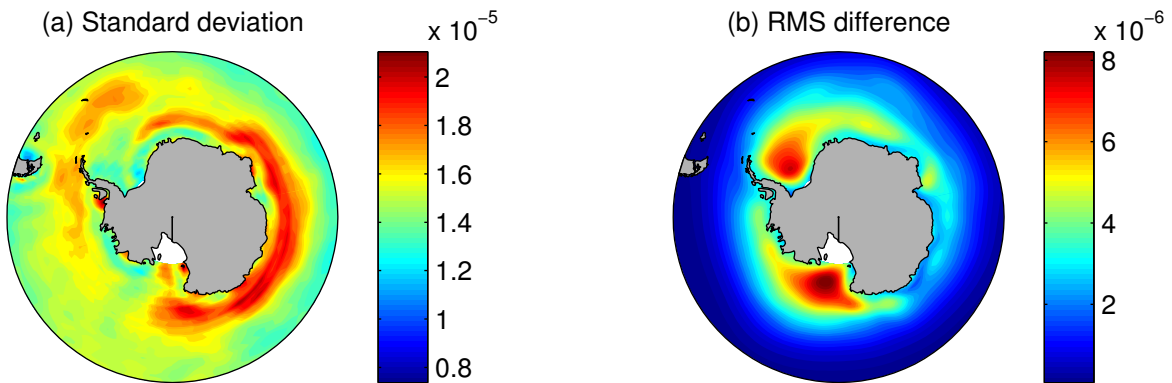


Figure 5: Standard deviation of NCEP wind curl (panel a) and RMS of the difference between the original NCEP wind curl and the adjusted wind curl (panel b). The units are s^{-1} .

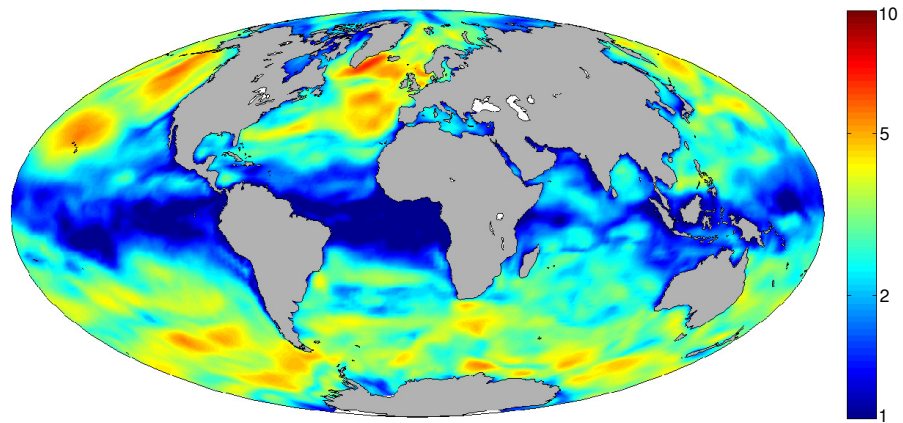


Figure 6: Wind speed ensemble standard deviation in m/s (2007-02-21).

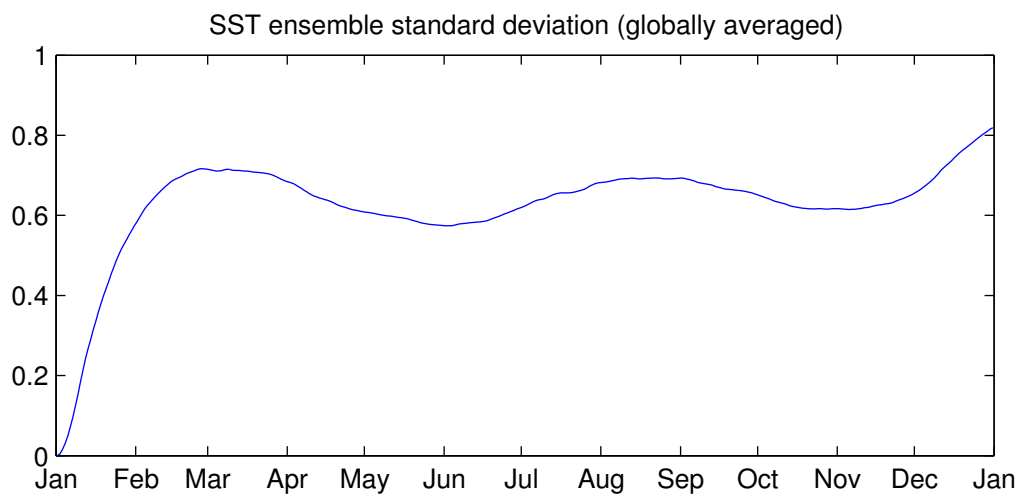


Figure 7: Globally-averaged SST ensemble standard deviation ($^{\circ}\text{C}$). The spread is first computed for every model grid point and then averaged spatially.

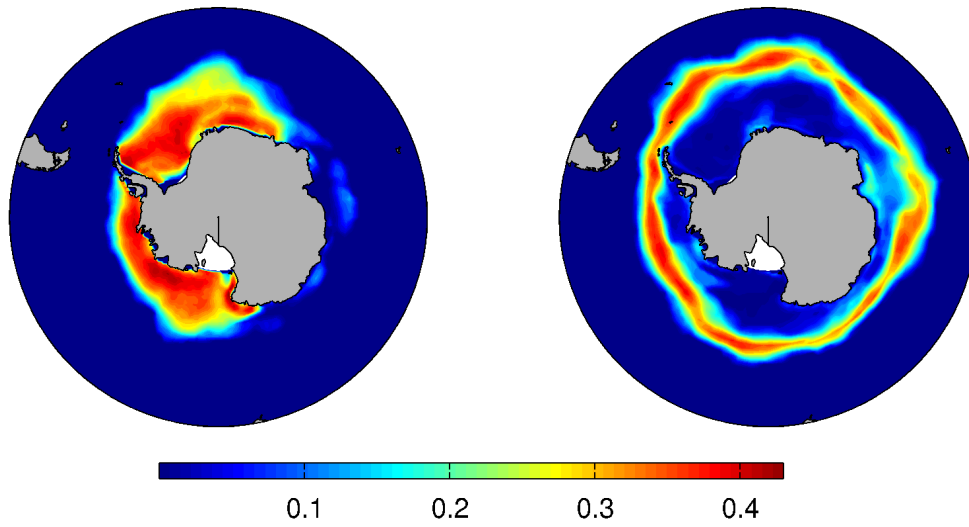


Figure 8: Sea ice concentration standard deviation at the minimum sea ice extent (2007-02-21, left panel) and during the maximum sea ice extent (2007-09-06, right panel)

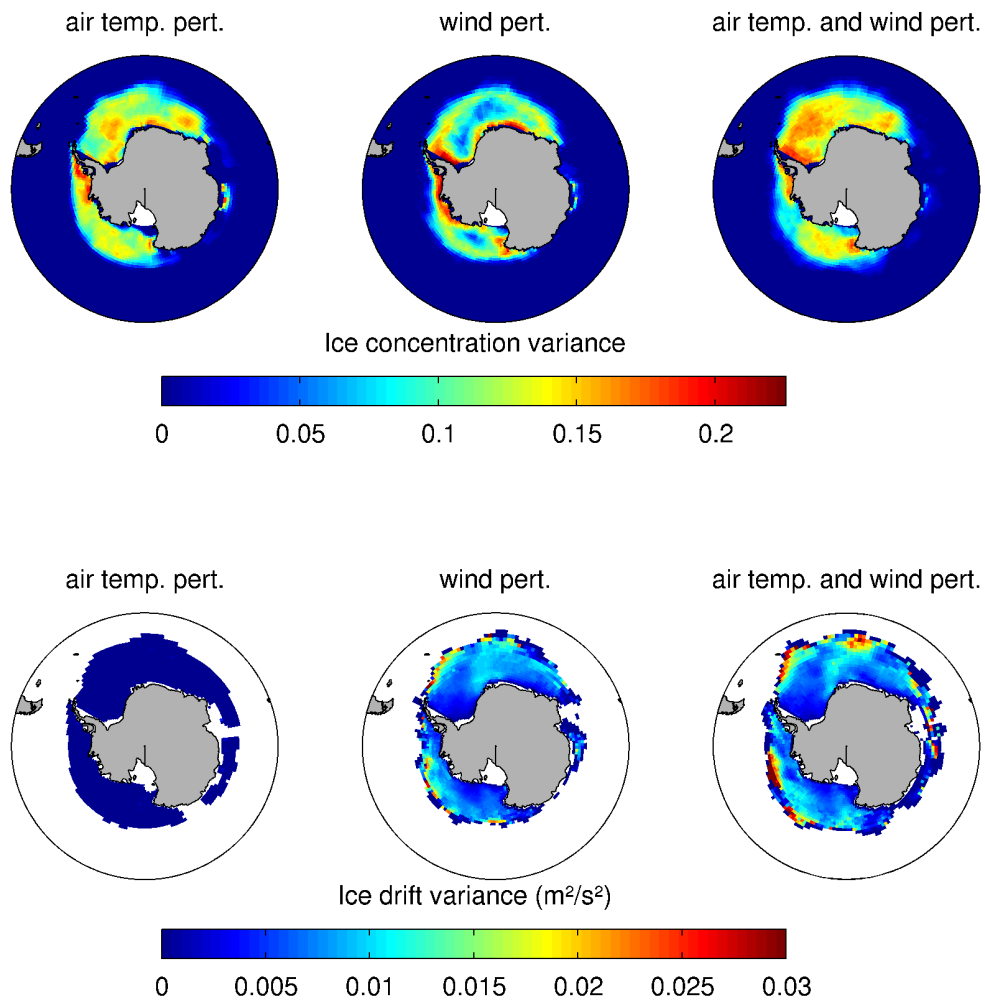


Figure 9: Ensemble variances of sea ice concentration (upper row) and sea ice drift (lower row) based on only air temperature perturbations, wind field perturbations or both. The ensemble variance corresponds to the starting day of the assimilation experiment (1985-01-01).

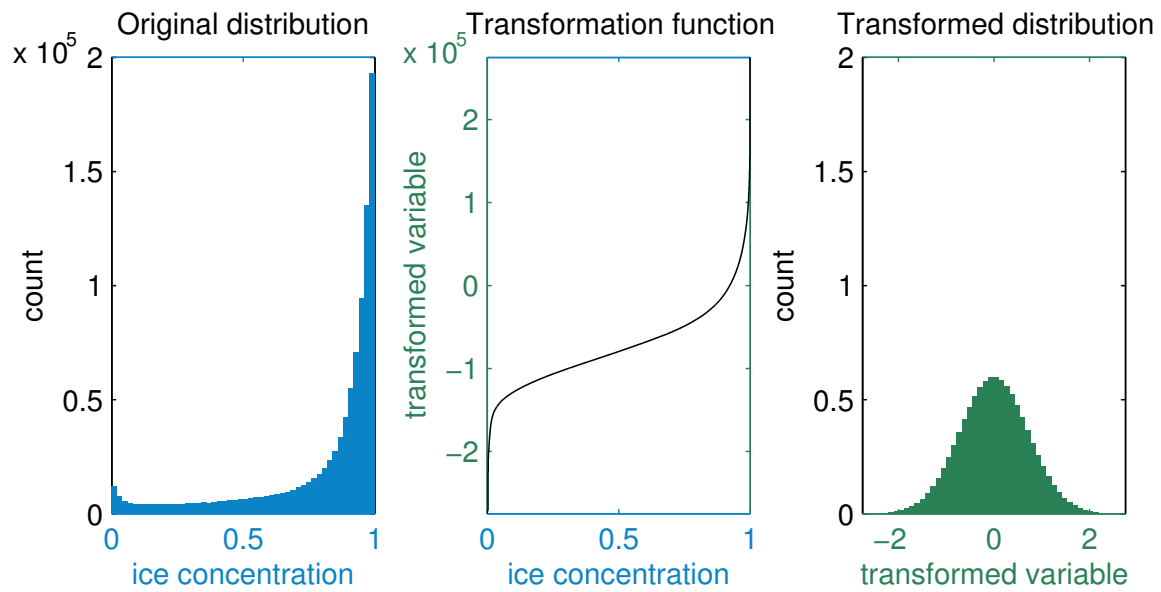


Figure 10: Illustration of the Gaussian anamorphosis: The left panel shows the original histogram of sea ice concentration, the middle panel represents the transformation function and the right panel is the resulting histogram.

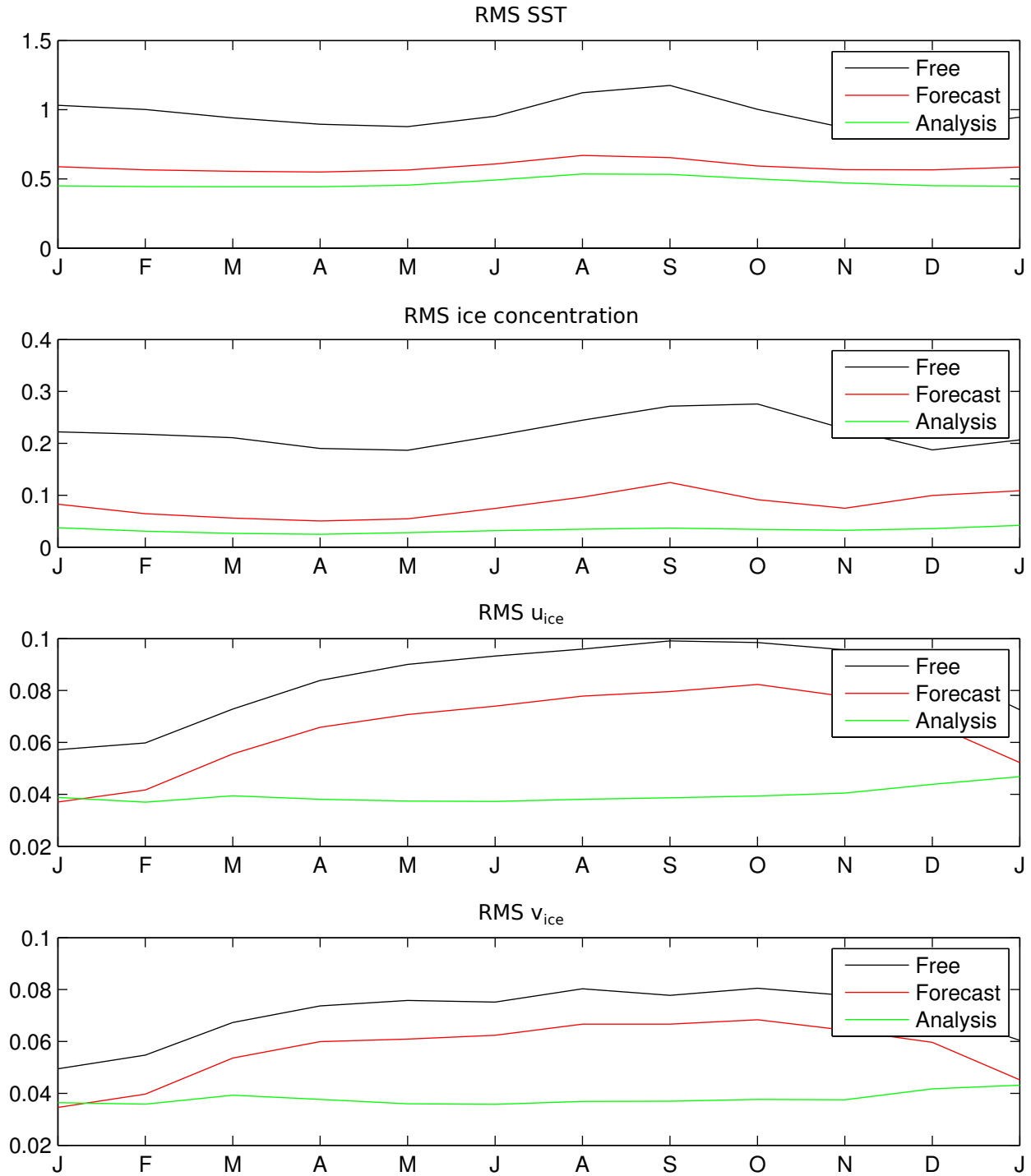


Figure 11: RMS error of the free running model and the model with assimilation (forecast and analysis) compared to the assimilated data for every month (x-axis) and averaged over all years.

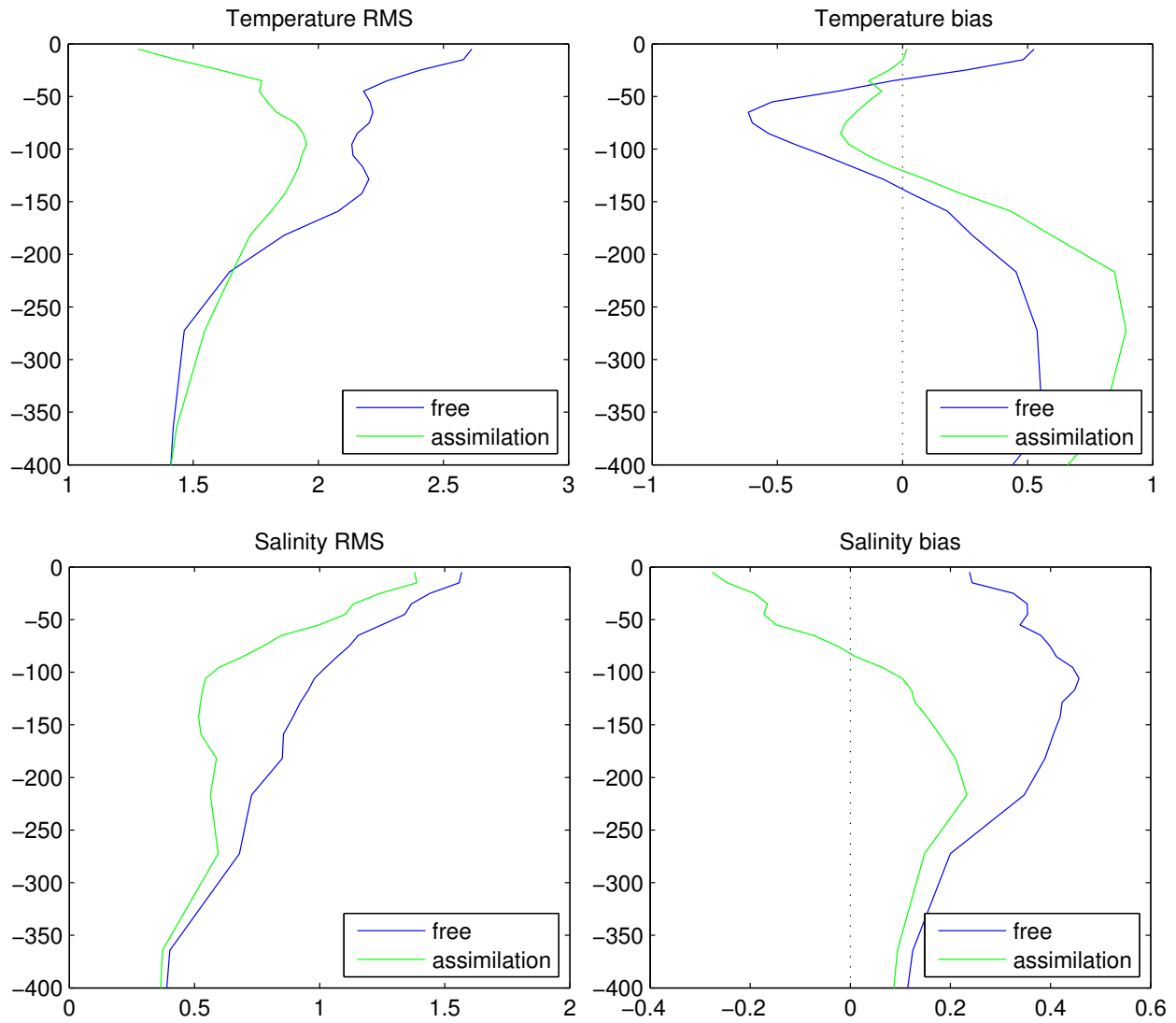


Figure 12: Validation with World Ocean Database using all observation from 1985-2006. The x-axis is temperature (upper row) or salinity (lower row) and the y-axis is depth.

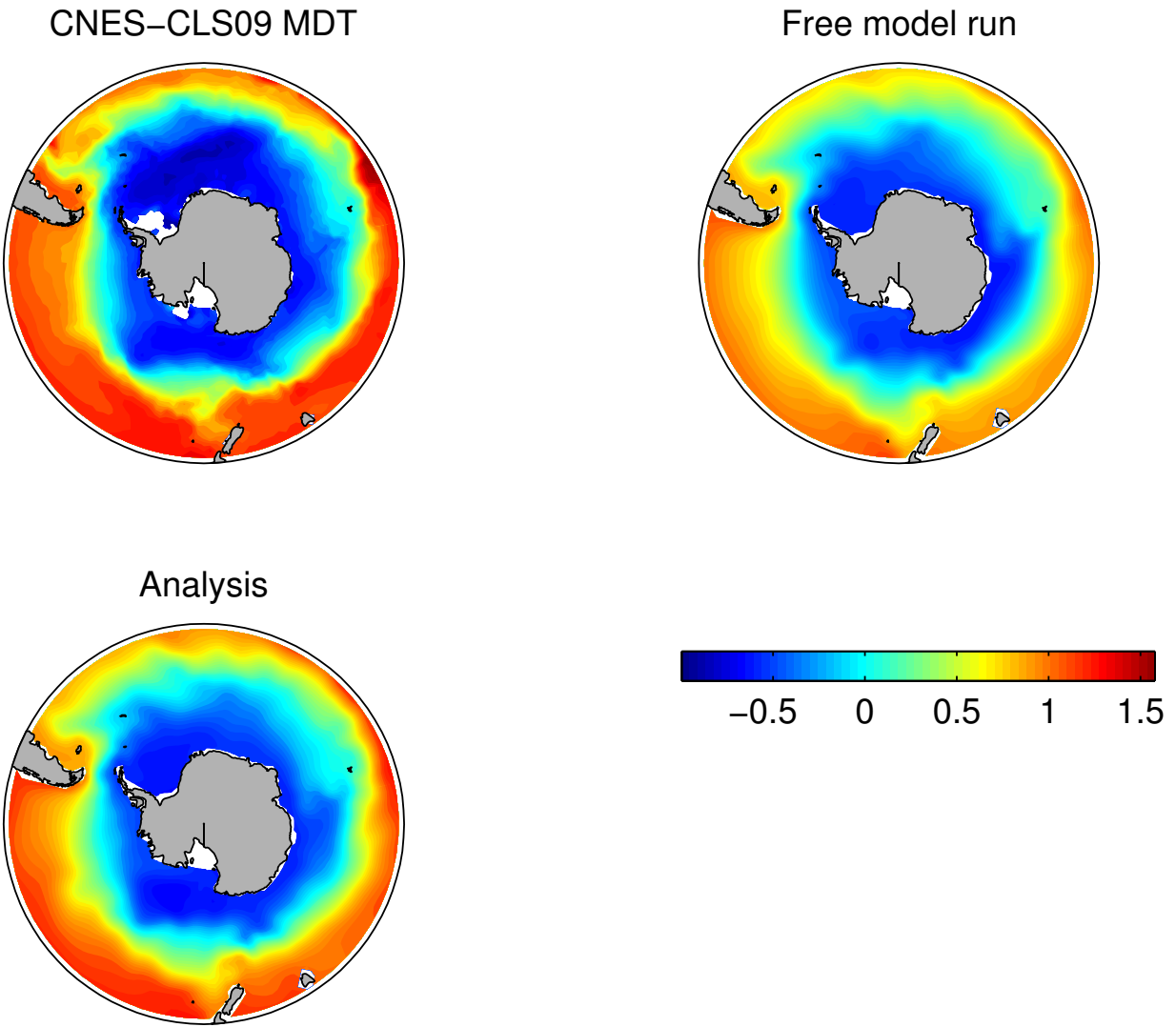


Figure 13: Comparison of mean SSH from observations and from the model (without and with assimilation). The spatial average of the shown domain was removed.

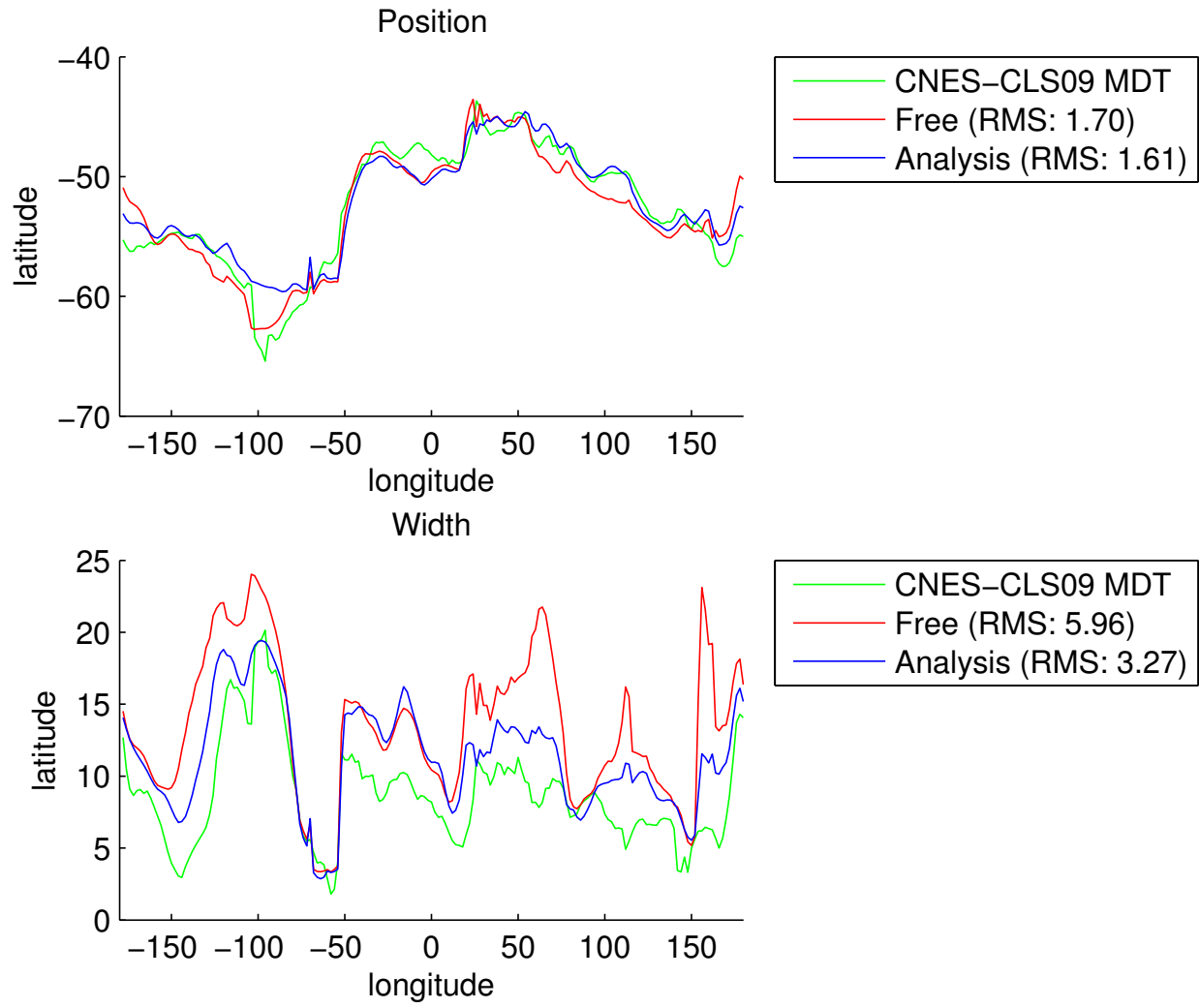


Figure 14: Position and width of the mean SSH front

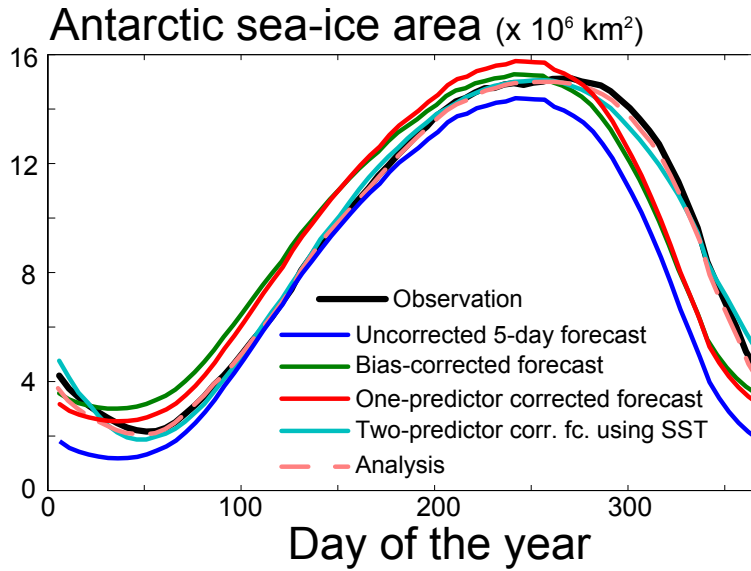


Figure 15: Antarctic sea ice area as a function of the day of the year averaged over the period 1985-2007. Shown are the observation, the reanalysis, the uncorrected 5-day forecast and different forecasts corrected with post-processing techniques.

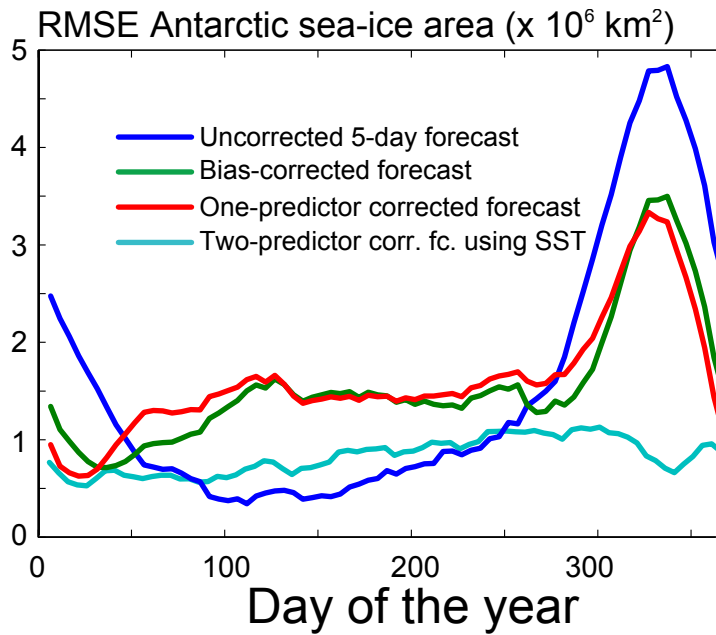


Figure 16: Root Mean Squared Error (RMSE) of the Antarctic sea ice area a function of the day of the year, averaged over the period 1985-2007, for the uncorrected 5-day forecast and different forecasts corrected with post-processing techniques.

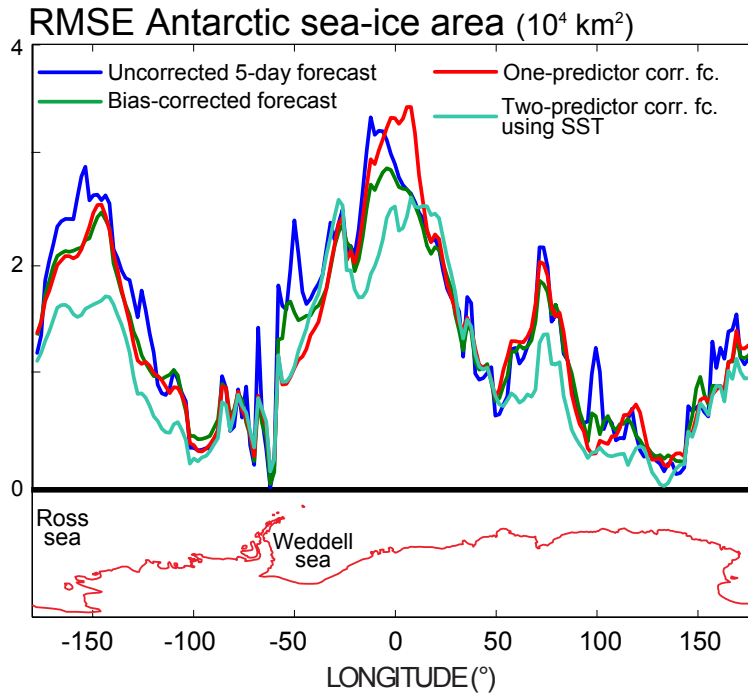


Figure 17: Root Mean Squared Error (RMSE) of the Antarctic sea ice area as a function of longitude for the uncorrected 5-day forecast and different forecasts corrected with post-processing techniques. The longitudinal spacing is 2° and the sea ice area at a certain longitude is the total sea ice area in a range of 2° east from that longitude (all south of 50°S).